nature communications

Article

https://doi.org/10.1038/s41467-025-56718-9

Single-molecule junctions map the interplay between electrons and chirality

Received: 10 July 2024

Accepted: 28 January 2025

Published online: 19 February 2025

Check for updates

Anil-Kumar Singh[1], Kévin Martin[2], Maurizio Mastropasqua Talamo[2], Axel Houssin[2], Nicolas Vanthuyne[3], Narcis Avarvari[2] ✉ & Oren Tal[1] ✉

The interplay of electrons with a chiral medium has a diverse impact across science and technology, influencing drug separation, chemical reactions, and electronic transport[1-30]. In particular, electron-chirality interactions can significantly affect charge and spin transport in chiral conductors, making them highly appealing for spintronics. However, an atomistic mapping of different electron-chirality interactions remains elusive. Here, we find that helicene-based single-molecule junctions behave as a combined magnetic-diode and spin-valve device. This dual-functionality enables the identification of an atomic-scale coexistence of different electron-chirality interactions: the magnetic-diode behavior is attributed to an interaction between electron's angular momentum in a chiral medium and magnetic fields, whereas the spin-valve functionality is ascribed to an interaction between the electron's spin and a chiral medium. This work uncovers the coexistence of electron-chirality interactions at the atomic-scale, identifies their distinct properties, and demonstrates how integrating their functionalities can broaden of the available methods for spintronics.

The interactions between electronic angular momentum, whether in a spin or orbital form, and a chiral medium hold diverse fundamental and practical implications. For example, these interactions are directly associated with molecular recognition, charge transfer in biosystems, chemical reactions, drug purification, and, foremost, with electronic transport in chiral conductors across all relevant scales and dimensions, down to individual molecules[1–30]. As a fundamental symmetry-related subject with broad impact, the details of these interactions have been subjected to extensive research[1–51]. However, an atomistic picture of the interplay between electronic angular momentum and a chiral medium remains elusive, along with its full potential for spintronic manipulations.

In the last two decades, a large set of phenomena related to electron transport and transfer in chiral conductors has been studied experimentally. The observed phenomena have been typically attributed to one of two general effects: the chiral-induced spin selectivity (CISS)[1,5–9,12,14,15,19–23,25–51] and the electrical magnetochiral anisotropy (EMCA, sometimes denoted as eMChA)[2–4,10,11,13,16–18,21,23,24,43,47,49]. In the former case (CISS; Fig. 1a), specifically in the context of electron transport, the magnetic moment of an electron moving in a chiral conductor interacts with the chiral system. Depending on the conductor's chirality and the direction of the electron velocity, this interaction promotes the transport of electrons with one spin direction (either parallel or antiparallel to the velocity) and suppresses the transport of electrons with the opposite spin direction. Thus, for a given chirality and current direction, the electronic current is dominated by one spin population. In the latter case (EMCA; Fig. 1b) that to date has not been identified in atomic-scale systems, the angular momentum[2,49] of an electron moving in a chiral system is affected by the chiral landscape. The interaction between the resulted angular momentum and an external magnetic field, parallel or antiparallel to the electron's velocity, promotes or suppresses electron transport. In this case, the conductor's resistance is decreased or increased by the EMCA effect depending on the chirality of the system, the current

[1]Department of Chemical and Biological Physics, Weizmann Institute of Science, Rehovot, Israel. [2]Univ Angers, CNRS, MOLTECH-Anjou, SFR MATRIX, Angers, France. [3]Aix Marseille Univ, CNRS, Centrale Med, UAR 1739, FSCM, Chiropole, Marseille, France. ✉e-mail: narcis.avarvari@univ-angers.fr; oren.tal@weizmann.ac.il

https://doi.org/10.1038/s41467-025-56718-9

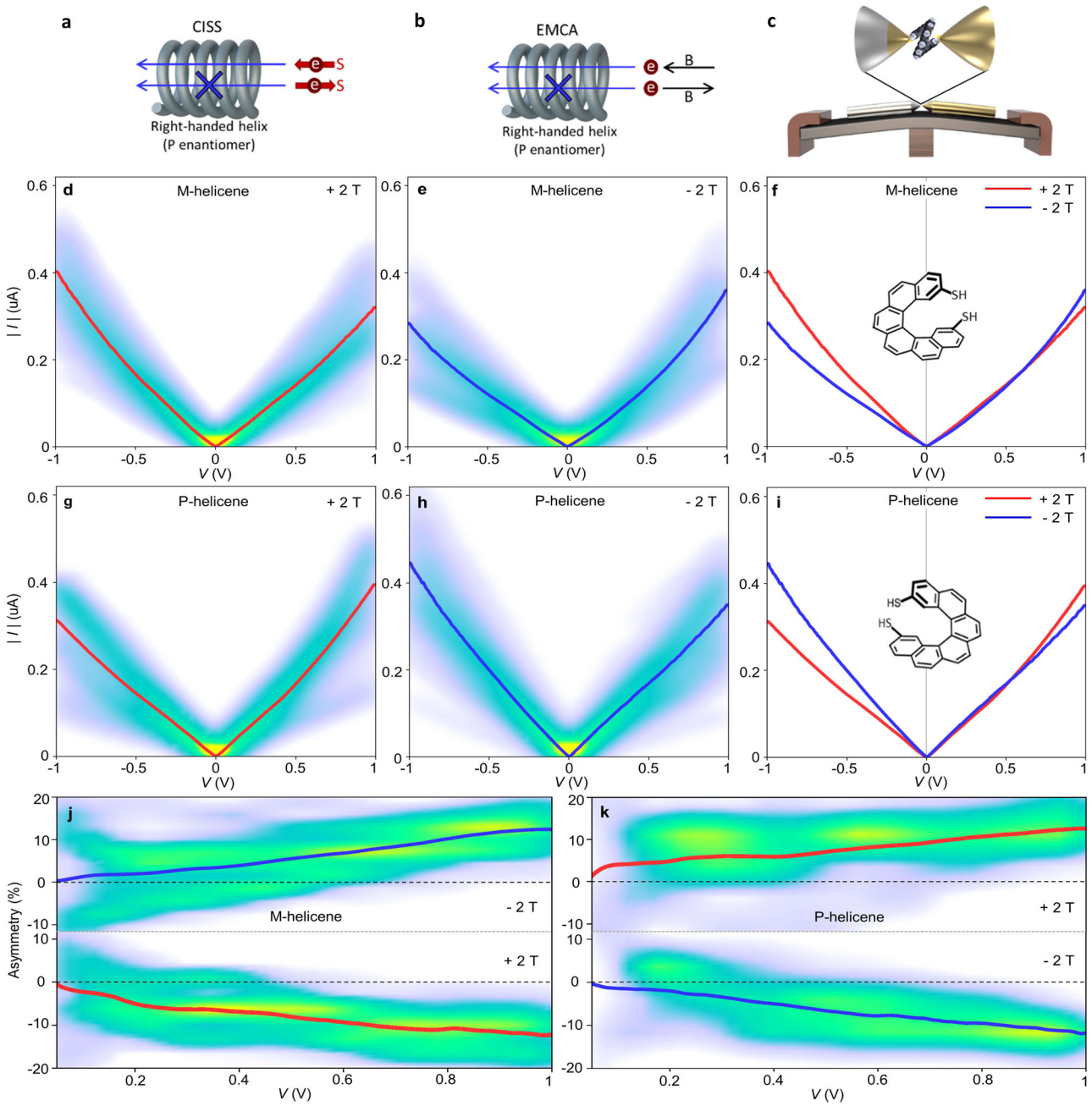

Fig. 1 | Current-voltage analysis of helicene molecular junctions under magnetic fields. a Illustration of chiral-induced spin selectivity (CISS). **b** Illustration of electrical magnetochiral anisotropy (EMCA). Here, the helix indicates a chiral conductor, red circles - electrons (e), red arrows—spin (S), blue arrows—electron transport directions, black arrows—magnetic field (B) directions. **c** Illustration of a break-junction setup and a helicene molecular junction. **d** Histogram and an average of current in absolute values as a function of voltage ($|I|$–V curves) for Ni(Au)/M-helicene/Au junctions under +2 T magnetic field, parallel to the junction. Ni(Au) refers to a Ni electrode wet by Au. **e** The same under −2 T magnetic field antiparallel to the junction. **f** Average of absolute value of current as a function of voltage for Ni(Au)/M-helicene/Au junctions under parallel and antiparallel +2 T and −2 T magnetic fields. **g**–**i** The same as (**d**–**f**) but for Ni(Au)/P-helicene/Au junctions. The standard error of the current [(standard deviation)/$\sqrt{\#\text{ of curves}}$] in (**d**) to (**i**) is smaller than the curve width. **j** Asymmetry as a function of voltage magnitude for Ni(Au)/M-helicene/Au junctions under the mentioned opposite magnetic fields. Asymmetry is defined as $\text{Asymmetry} = 100 \cdot [|I(+V)| - |I(-V)|]/[|I(+V)| + |I(-V)|]$. **k** The same as in (**j**), but for Ni(Au)/P-helicene/Au junctions. The number of examined molecular junctions (and corresponding I–V curves) in each case varies between 251 to 377.

direction, and the external magnetic field orientation. The CISS effect is expected to be detected experimentally when time-reversal symmetry breaks, while for the EMCA effect this condition already holds[47].

In this work, we reveal the simultaneous occurrence of the EMCA and CISS effects at the atomic-scale and characterize their properties at the limit of quantum transport. Specifically, we find that single-molecule junctions based on helicene molecules behave as a merged magnetic-diode and spin-valve device, due to a coexistence of the EMCA and CISS effects. The distinct nature of these effects is unveiled by their different response to applied magnetic fields, and electrodes composed of metals with different spin-orbit coupling (SOC). We find no apparent coupling between the EMCA and CISS effects and identify the conditions in which their magnitude is equal. We uncover an unknown response of the EMCA effect to SOC, and the absence of a similar response for the CISS effect. This important observation can limit the range of relevant theoretical models for the two effects. Our

https://doi.org/10.1038/s41467-025-56718-9

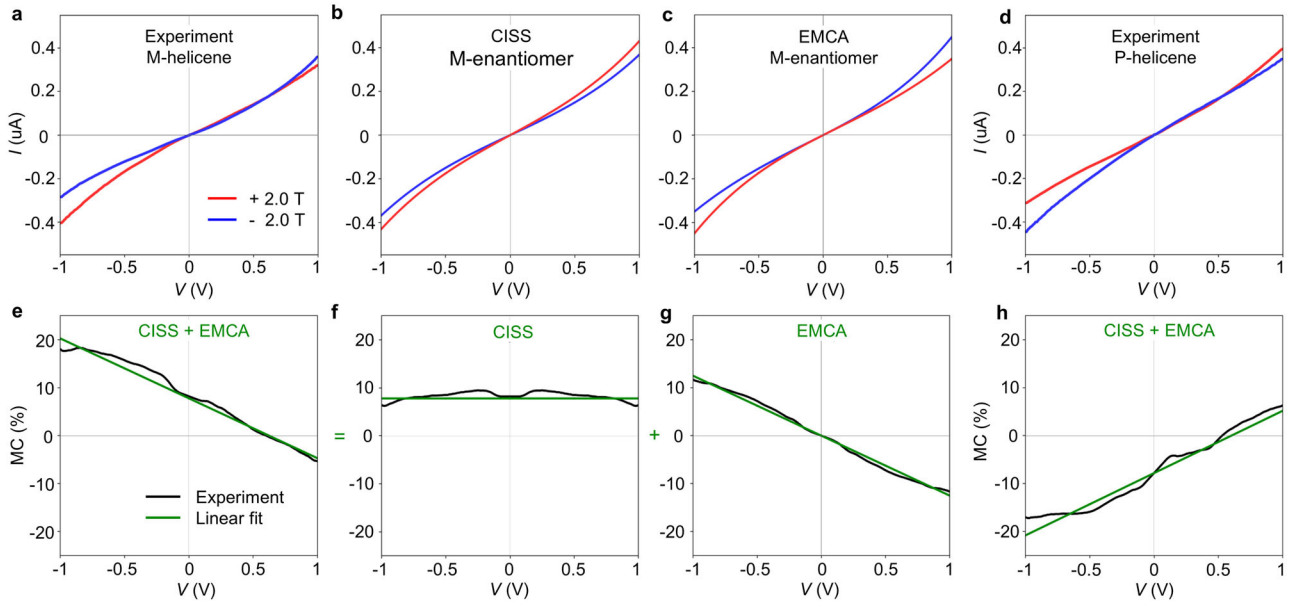

Fig. 2 | Magnetoconductance in view of the CISS and EMCA effects. a Measured average *I*–*V* curve for hundreds of Ni(Au)/M-helicene/Au junctions. Simulated *I*–*V* curve for the CISS effect (**b**), and the EMCA effect (**c**). For details about the model underlying (b,c), see Supplementary section 3. **d** Measured average *I*–*V* curve for hundreds of Ni(Au)/P-helicene/Au junctions. The standard error of the current in (**a**,**d**) is smaller than the curve width. **e** Average magnetoconductance (MC) (black) based on measured data from (**a**) for M-helicene junctions. The green curve represents a linear fit. **f** Symmetric component (black) of the MC in (**e**), and a linear fit (green). **g** Antisymmetric component (black) of the MC in (**e**), and a linear fit (green). **h** Average MC (black) based on measured data from (**d**) for P-helicene junctions. The green curve is not a fit to the data in (**h**), but a mirror inversion of the fit for the measured MC of the M-helicene junctions seen in (**e**). Note the agreement between the inverted curve based on data obtained in a set of experiments for the M-helicene junctions and the data obtained in independent set of experiments for the P-helicene junctions. The MC in (**e**) and (**h**) is obtained from *I*–*V* data above ±100 mV for robust results. The number of examined molecular junctions in each case varies between 251 and 377.

work maps the different contributions that dominate the interplay between electrons and a chiral medium at the atomic scale. The found coexistence of the CISS and EMCA effects at this scale presents opportunities for a broader range of spintronic manipulations in miniaturized systems, leveraging the different nature of each effect.

We use single-molecule junctions prepared in a break-junction setup at 4.2 K (Fig. 1c[52,53]). The junctions include a Ni electrode as a source or drain for spin-polarized current, a counter electrode made of Au, Ag, or Cu, and an unprecedented 2,2′-dithiol-[6]helicene (helicene hereafter) as a chiral molecular bridge (see Supplementary Section 1 for synthesis and characterization, Figs. S1–S6, and Tables S1–S5). The choice of the molecule was motivated by the well-known affinity of thiol groups for the coinage metals and by the robust helical chirality of the helicene framework[54]. Before the molecules are introduced, the contact between the electrode tips is repeatedly broken and reformed in sub-atomic precision. This process wets the Ni tip with the softer metal of the counter electrode to have two atomic-scale apexes made of the softer metal[52]. Next, the helicene molecules are introduced into the cold junction by in-situ sublimation from a local source during repeated junction breaking and squeezing[53]. We use either the P-enantiomer of helicene with a clockwise helicity or the M-enantiomer with an anticlockwise helicity (Fig. 1, insets). The described junction fabrication and the following measurements are done in a cryogenic temperature and ultra-high vacuum conditions that minimize unwanted contaminations. See details in "Methods" and Supplementary Section 2.

Results

Current–voltage curves under magnetic fields, asymmetry, and magnetoconductance

Figure 1d–i presents histograms and average current in absolute values, as a function of applied voltage (|*I*|-*V* curves) measured for hundreds of molecular junction realizations. Before each measurement, the two electrode apexes are squeezed against each other and then stretched to reform a new molecular junction in order to sample the span of different molecular junction configurations. Separate sets of |*I*|-*V* measurements were performed for molecular junctions based on M (Fig. 1d, e) and P (Fig. 1g, h) enantiomers. During the measurements, a constant magnetic field of +2 or −2 Tesla (T) was applied to align the Ni magnetization parallel or antiparallel to the junction's axis. Consequentially, a spin-polarized current is generated at a finite voltage with a dominant population of spins aligned either antiparallel or parallel to the junction's axis. To have a better comparison between these cases, the average |I|-V curves for opposite magnetic fields, are presented together in Fig. 1f, i, for each enantiomer (refer to Figures S7–S13 for complementary information related to Fig. 1). Interestingly, the |I|-V curves are asymmetric, revealing current rectification or diode-like behavior. Namely, the current magnitude is different for a positive and negative voltage. For a given enantiomer, the asymmetry is inverted when the magnetic field direction is reversed (blue versus red in Fig. 1f, i). Moreover, for a given magnetic field (e.g., blue curves in Fig. 1f, i), the asymmetry is inverted when opposite molecular chirality (P or M) is used. This is quantitatively summarized in Fig. 1j, k, by asymmetry histograms and average asymmetry as a function of voltage (see Fig. 1 caption for asymmetry definition). The observed inversion of asymmetry when opposite chirality or magnetic field direction are used rules out the possibility of an asymmetric junction structure as the source of asymmetry in the |*I*|–*V* curve. Thus, the origin of the diode-like behavior of the helicene junctions is clearly related to the application of magnetic fields and the molecule's chirality.

CISS and EMCA in current–voltage curves and magnetoconductance

The identified current rectification (e.g., Fig. 2a, in polar *I*–*V* presentation) stands in contrast to the characteristics of *I*–*V* measurements reported in previous experiments related to the CISS effect across a wide range of systems. These systems include a chiral

conducting medium positioned between ferromagnetic and non-ferromagnetic electrodes[6,19–21,26,27,29]. Irrespective of the diverse architectures and materials used, in all these cases the reported response of the *I*–*V* curves to opposite magnetization or chirality is symmetrical in the following sense. The current magnitude in one curve is always larger than that of the other curve, regardless of voltage polarity as illustrated in Fig. 2b. This behavior was attributed to the injection of spins with opposite orientations at positive and negative applied voltages[55]. We include in this definition also previously reported asymmetric *I*–*V* curves resulting from uneven voltage drops across an asymmetric junction structure, where the current magnitude may differ for opposite voltages. However, it consistently remains larger for a specific chirality and magnetic field direction when compared to their opposite counterpart[6,29,56]. In contrast to the findings related to the CISS effect, the EMCA effect induces a suppression of resistance for one voltage polarity and an enhancement in resistance for the opposite voltage polarity[2–4]. Specifically, for a given chirality and magnetic field orientation, the contribution to resistance (or conductance, which is 1/resistance) by the EMCA effect changes its sign, depending on the current direction. This is translated into current rectification and an asymmetric *I*–*V* curve[11,24,47,49,57], as exemplified in Fig. 2c. However, also this behavior shows merely partial resemblance to our measurements (e.g., Fig. 2a, d).

To understand the observed *I*–*V* behavior for the helicene junctions, we turn to magnetoresistance (MC), defined as: $MC = [G\uparrow(V) - G\downarrow(V)]/[G\uparrow(V) + G\downarrow(V)]$, where $G_i = I_i/V$ is the conductance measured under positive (i = ↑) and negative (i = ↓) magnetic fields. Figure 2e, shows in black the MC obtained from the *I*–*V* curves in Fig. 2a for M-helicene junctions. The MC curve can be decomposed into symmetric $MC(+V) + MC(-V))/2$) and antisymmetric $MC(+V) - MC(-V))/2$ components, presented in black in Fig. 2f and g, respectively. Ignoring the fine structure of the symmetric MC curves in Fig. 2f, we can find a linear fit (green) to this MC component. According to the MC definition, a symmetric MC implies an *I*–*V* curve with a current magnitude always larger for a positive magnetic field compared to the *I*–*V* curve for a negative magnetic field. In fact, using the MC definition, the fit in Fig. 2f can be produced by the *I*–*V* curves presented in Fig. 2b that illustrate the CISS response (see Supplementary Section 3 for the phenomenological model used to produce Fig. 2b). Therefore, the MC symmetrical response to magnetic field is a typical signature for the CISS effect. The antisymmetric MC component in Fig. 2g is also fitted to a linear function (green). In contrast to the above case, the antisymmetric MC component indicates for a positive magnetic field an *I*–*V* curve with a current magnitude smaller for one voltage polarity and higher for the other polarity, and vice versa for the opposite magnetic field. This description aligns with the behavior of the *I*–*V* curves shown in Fig. 2c that illustrate the EMCA response. These *I*–*V* curves are related to the fit in Fig. 2g through the MC definition (Supplementary Section 3), and the antisymmetric MC response to magnetic field is therefore associated with the EMCA effect. Since the sum of the green fits in Fig. 2f, g yields the fit to the total MC in Fig. 2e, the general behavior of the experimentally obtained MC in Fig. 2e can be explained by the contribution of both effects: the CISS accounts for the MC shift (finite MC intercept), while the EMCA introduces the MC tilting (non-zero MC slope), and the peculiar behavior of the measured *I*–*V* curves in Fig. 2a is an outcome of the concurrent contributions from the CISS (Fig. 2a) and EMCA (Fig. 2a) effects. Focusing on the *I*-*V* curves and the resulted MC for the P-helicene junctions presented in Fig. 2d and h, respectively, the green curve in Fig. 2h is not a fit to this graph. Interestingly, it is the linear fit seen in Fig. 2g yet with an inverted intercept and slope signs, revealing a remarkable agreement with the measured data for P-helicene junctions in evidently independent experiments. See Supplementary Section 3 for additional details, and a comparison of the symmetric and antisymmetric MC components for M- and P-helicene junctions. We note that the insensitivity of the symmetric MC component, associated here with the CISS effect, to the applied voltage is consistent with previous reports on the CISS effect[19,20,56,58–61] (in most of these reports, the definition of spin polarization is equivalent to our definition of MC).

The influence of magnetic field magnitude

As mentioned, the EMCA effect arises in the presence of an external magnetic field. In contrast, the CISS effect is not expected to be influenced by such fields, except for a negligible influence from Zeeman splitting. Figure 3a–i presents the $|I|$-*V* curves, asymmetry, and MC in three different magnetic fields. Here, magnetic fields above 2 T were considered to ensure magnetization saturation even at the Ni atomic apex, and higher fields than 4 T were avoided due to expected contributions from high-order corrections to the EMCA effect[3,7,24]. While there are evident differences between the curves, to get quantitative information we first focus on the asymmetry at 1 V as a function of magnetic field as presented in Fig. 3j, which reveals a clear linear dependence. The asymmetry is proportional to the conductance difference between positive and negative voltage (Supplementary Section 4), which is expected to be linear and reduced to zero in the absence of magnetic field for the EMCA effect[2,3]. Applying linear fits (red) to the data at negative and positive magnetic field, yields similar slopes and intercepts within the measurement uncertainty listed in the caption of Fig. 3. This similarity allows us to consider the intercepts as reliable evidence of a finite EMCA at zero applied magnetic field. This behavior may originate from the presence of the Ni electrode, considering the Ni-induced finite magnetic field even when the external field is nullified, and other possible contributions. A detailed identification of the different mechanisms in which a ferromagnetic electrode can influence the EMCA effect requires further specialized studies. However, in the context of this work, we repeated the measurements without the Ni electrode for an ensemble of Au/M-helicene/Au junctions at ± 2 T (Fig. S13). We found that the MC shift attributed to the CISS effect is essentially nullified in the absence of spin injection, as expected. Interestingly, comparing Fig. S13d to Fig. 1j, the asymmetry attributed to the EMCA effect is clearly reduced in the absence of the Ni electrode, corroborating the conclusion that the presence of the Ni electrode affects the EMCA effect.

Plotting in Fig. 3k the detected MC shift as a function of magnetic field magnitude reveals that it is not sensitive to the field, as expected for the CISS effect (see Supplementary Section 5). The asymmetry response to magnetic fields and the lack of detected influence of the field on the MC shift, support the earlier conclusion that the asymmetry is an outcome of the EMCA effect, while the observed MC shift is a consequence of the CISS effect. The zero MC at a positive voltage signifies a specific point where the influence of the EMCA and the CISS effects is equal and opposite, resulting in MC nullification (Supplementary Section 3). This point shifts to a lower voltage with an increase in magnetic field, as expected in view of the EMCA response to magnetic field strength. Interestingly, the linear response of the asymmetry to magnetic fields and the absence of any detected effect of magnetic fields on the MC shift suggest that within our experimental sensitivity there is no coupling between these manifestations of the CISS and EMCA effects.

The influence of metal electrodes with different spin-orbit coupling

Examining the response of the two effects to a common variable can further test their coexistence while providing insights into the distinct nature of each effect. Below, we consider the influence of different non-ferromagnetic electrodes made of Cu, Ag, and Au, having in mind their different SOC with increasing magnitude: Cu<Ag<Au[62]. In all three cases, the molecular junctions are characterized by a similar conductance around $5{\cdot}10^{-3}\,G_o$ (Fig. S7). Figure 4a–c presents the measured

https://doi.org/10.1038/s41467-025-56718-9

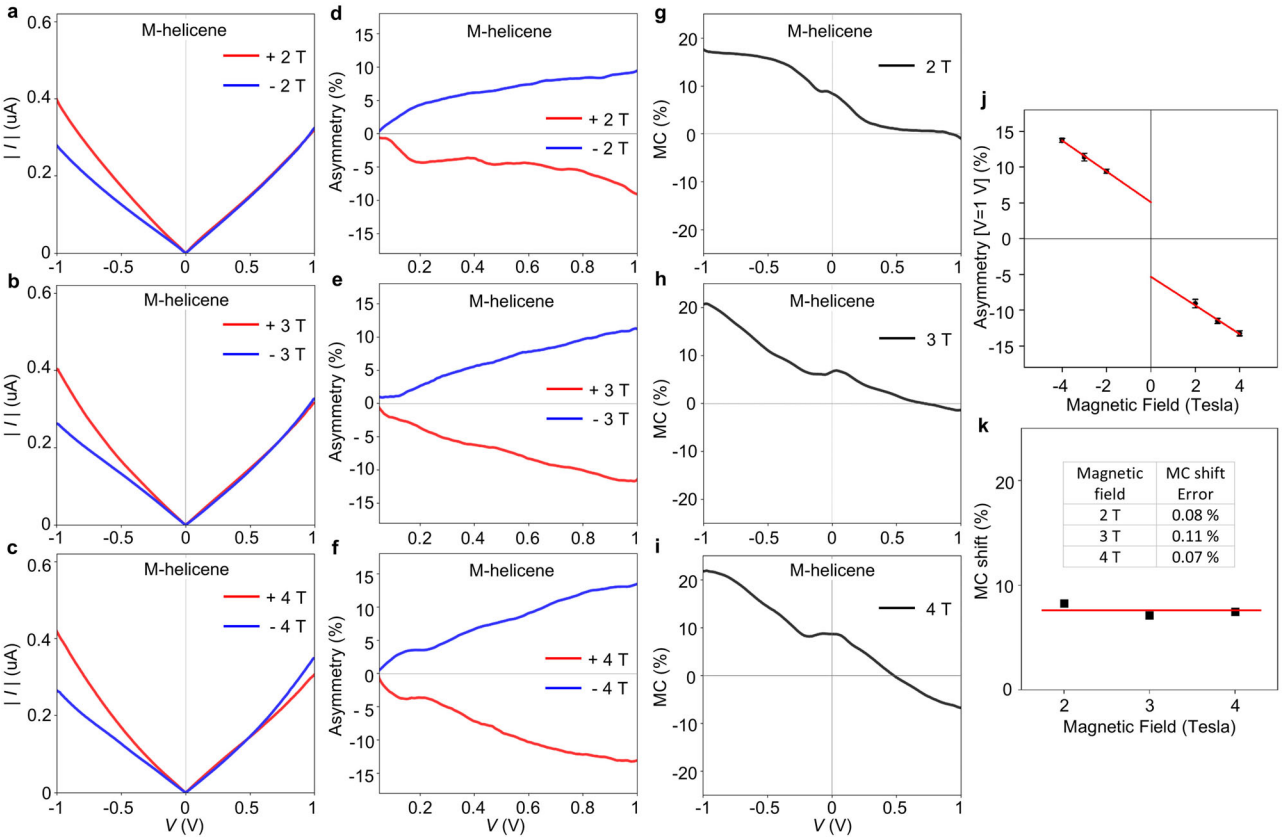

Fig. 3 | Asymmetry and MC analysis at different magnetic fields. a–c Average current (in absolute values) as a function of applied voltage for Ni(Ag)/M-helicene/Ag junctions at different applied magnetic fields. The standard error of the current is smaller than the curve width. **d–f** Average asymmetry as a function of applied voltage magnitude at different applied magnetic fields. **g–i** Average MC as a function of applied voltage at different magnitudes of magnetic field. The MC is obtained from I-V data at voltages above ±50 mV. **j** Asymmetry at 1 V as a function of magnetic field. Red curves are linear fits with slopes and intercepts of: −2.2 ± 0.1 %/T and −5.1 ± 0.2 % for negative fields, and −2.0 ± 0.2 %/T and −5.3 ± 0.8 % for positive fields. **k** MC shift as a function of magnetic field magnitudes. The shift is obtained by the intercept of a linear fit to the MC data (see Supplementary section 5). The error bars for asymmetry and MC indicate the experimental uncertainty in view of the standard deviation of the measured currents. The number of examined molecular junctions in each case varies between 372 and 634. We study the response to magnetic field magnitudes using junctions based on Ag rather than Au. This choice is motivated by the tendency of Au to form atomic chains, which enhances result variability and complicates the analysis, especially when minor trends should be carefully detected. See Fig. S16 for corresponding $|I|$-V and asymmetry histograms.

average $|I|$-V curves for the three cases when applying parallel and antiparallel magnetic fields for M-helicene junctions (see Fig. S18 for a similar analysis of P-helicene junctions). The $|I|$-V response to magnetic fields varies among junctions based on the three different metals. Examining in Fig. 4d–f the resulting asymmetry, we find a monotonous increase in its magnitude. Figure 4j summarizes the total asymmetry (sum of positive and negative asymmetry magnitudes) at 1 V for the three different metals, where a larger asymmetry is observed for metals that exhibit a larger SOC. Focusing on MC in Fig. 4g–i, the increased tilt observed along the Cu, Ag, and Au series is another manifestation of the mentioned asymmetry trend. However, the MC shift presented in Fig. 4k is not sensitive to the metal type (see Supplementary Sections 5 and 6).

The different response of asymmetry and MC shift to the metal type strengthen the conclusion that they stem from two different effects, in accordance with the accumulated indications presented above for the coexistence of the CISS and EMCA effects. The observed increase in asymmetry along the set of Cu, Ag, and Au provides the first systematic indication for a possible influence of SOC on the EMCA effect. This provides guidelines for a theoretical examination of the role of SOC in the EMCA effect, a dimension that is currently absent. The association of the CISS effect with MC shifts and the absence of a clear MC shift response in Fig. 4k (ignoring ~1% lower shift for Cu) suggest that at the limit of the measurement uncertainty, the CISS effect is not sensitive to the electrode's SOC or other variance between the used Au, Ag and Cu electrodes, in agreement with[14,16], where similar metals were used. Note that the slightly lower response for the Cu-based electrode is observed both here and in refs. 14,16. This contrasts the observations reported in ref. 27, where the use of an Al substrate led to a significantly lower MC compared to an Au substrate. We can point to one difference in the mentioned comparative analyses: all the mentioned metals have distinct SOCs, but Cu, Ag, and Au have dominant s frontier orbitals at the Fermi energy, in contrast to Al with dominant p on top of s frontier orbitals. These may indicate the sensitive role of the substrate's atomistic properties in determining the spin-dependent transport via metal-chiral molecule interfaces. Generally, if the CISS effect is indeed independent of the metal's SOC as observed here, it narrows down the range of theoretical explanations pertinent to the CISS effect in similar systems.

Discussion

The clear indications for the EMCA effect in the examined single-molecule junctions raise a question regarding the conditions in which this effect can be observed at the atomic or molecular scale. Previous I–V measurements in chiral molecular junctions were typically performed as a function of magnetization orientation of one of the electrodes in order to explore the CISS effect. In these studies, a planar multi-molecular geometry or a scanning probe microscope

https://doi.org/10.1038/s41467-025-56718-9

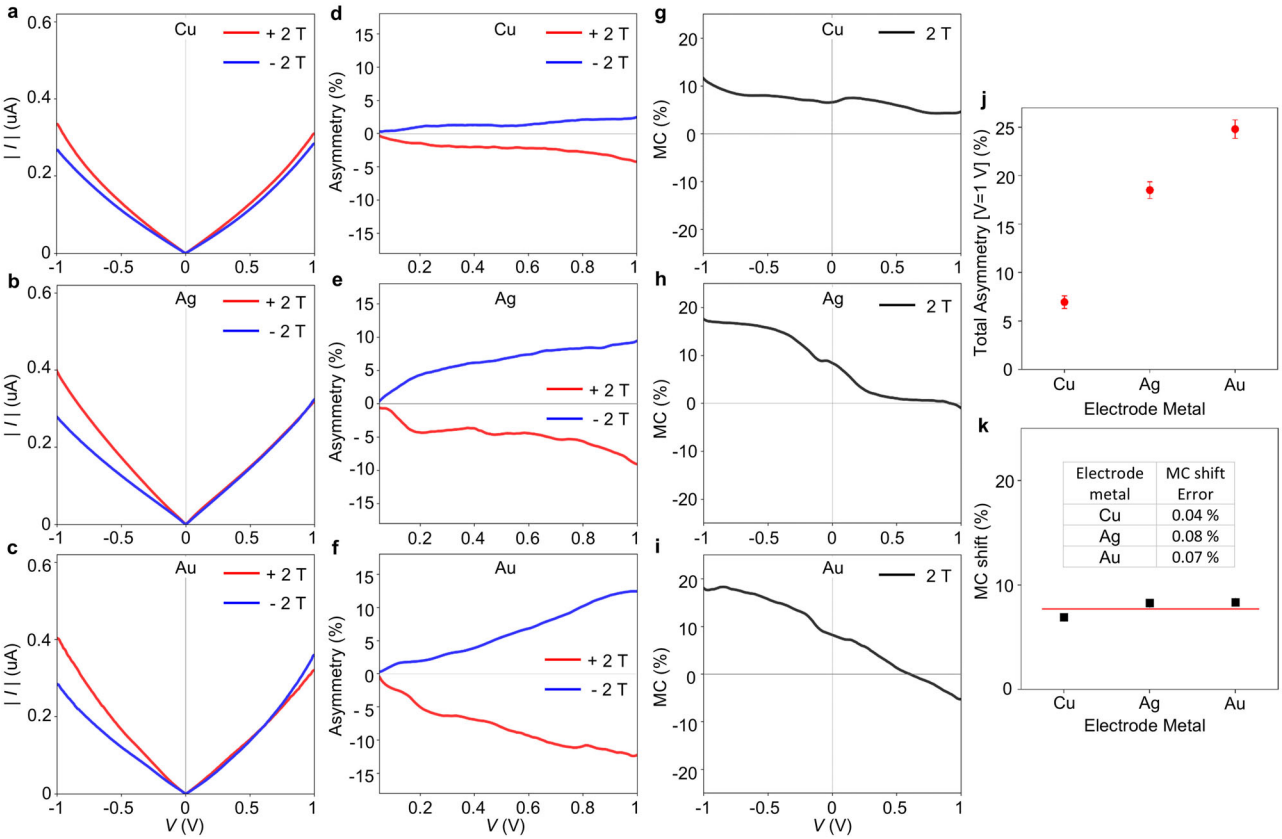

Fig. 4 | Asymmetry and MC response to different metal electrodes. a–c Average current (in absolute values) as a function of applied voltage for Ni(*X*)/M-helicene/*X* junctions, where *X* is Cu (**a**), Ag (**b**), and Au (**c**). The standard error of the current is smaller than the curve width. **d–f** Average asymmetry as a function of applied voltage magnitude for the same junctions as in (**a–c**), respectively. **g–i** Average MC as a function of applied voltage for the same junctions as in (**a–c**), respectively. The MC is obtained from *I–V* data at voltages above ±50 mV for Cu and Ag-based junctions, and ±100 mV for Au-based junctions. **j** Total asymmetry at 1 *V* for junctions based on different metals. **k** MC shift for junctions based on different metals. The shift is obtained by the MC-axis intercept of a linear fit to the MC data (see Supplementary section 5). The red curve represents the average value. The number of examined molecular junctions in each case varies between 316 and 443. The error bars for asymmetry and MC indicate the experimental uncertainty. See Figs. S16a,d,g, Fig. S17, and Fig. 1d,e,j for |*I*|-*V* and asymmetry histograms for the three cases. See Fig. S18 and Fig. S19 for a similar analysis of P-helicene-based junctions.

configuration was usually adopted, where a flat ferromagnetic thin film was used as a central component of one of the electrodes (e.g., refs. 6,20,29). These structures have essentially a negligible intrinsic magnetic field, ignoring the film's edges. In another example, the molecule was placed away from the ferromagnet[26]. Beyond a sizable magnetic field, a significant current density can also enhance the EMCA response[49]. While high current densities are not typical for multi-molecular junctions, they are expected for single-molecule junctions[29]. In fact, the combination of both: a sizable magnetic field, and a high current concentration, are met in our single-molecule junction experiments. In our setup, one of the electrodes is made of bulk Ni with an intrinsic magnetic field, and the junction is subjected to external fields of at least 2 T. Furthermore, the current concentration is around 10^7 A/cm^2. Therefore, we expect that the EMCA effect will be seen in chiral single-molecule junctions with similar current concentrations and magnetic fields. We could not find indications for the reduction in the CISS response when the voltage is reduced to 50 mV. This may seemingly violate the constraints set by time-reversal symmetry. According to the latter, the CISS should be nullified within the linear response regime[37,39,42,45,51]. Yet, our observations agree well with former measurements of a finite CISS response at low applied voltages across ferromagnet-based two terminal devices[63,64], thus providing guiding lines for theoretical descriptions of the CISS effect.

To conclude, in this work chiral single-molecule junctions are used to map the interplay of electrons and chirality at the atomic scale. This electron-chirality interaction dominates charge and spin transport in chiral materials. We uncover the simultaneous occurrence of the CISS and EMCA effects at the atomic scale, seen as a combined magnetic-diode-spin-valve spintronic functionality. Our analysis reveals no apparent coupling between these effects. Importantly, we find that metallic electrodes with different SOC affect the EMCA response, but not the CISS response. This work provides the first indication of the existence of the EMCA effect at the atomic scale and at the limit of quantum electronic transport. We further reveal an unknown SOC influence on the EMCA effect, offering a starting point for developing an atomistic EMCA theory, which is currently absent. The lack of substrate SOC influence on the CISS effect in electronic transport experiments can be used to narrow down the relevant atomistic mechanisms for this effect. Overall, the coexistence of the CISS and EMCA effects, both of comparable magnitude at the atomic scale, can expand the scope of spintronic functionalities in miniaturized systems by harnessing the unique characteristics of each effect.

Materials and methods

Sample preparation

The experiments are done in a special version of a mechanical controllable break-junction set-up (Fig. 1c) as described in detail in ref. 52, and briefly here. The samples consist of one electrode made of a Ni wire terminated with a tip and a second counter electrode made of an Au, Ag, or Cu wire also ended with a tip (purity: 99.994% (Ni), 99.998% (Au), 99.997% (Ag), 99.9999% (Cu), diameter: 0.1 mm, length: 6 mm, manufacturer: Alfa Aesar). The two wires are attached to a flexible

substrate composed of a phosphor-bronze plate (thickness: 1 mm) covered by an insulating Kapton film (thickness: 100 μm). Initially, the flexible substrate is bent, and subsequently, the two wires are attached to the bent substrate, with their tips oriented toward each other. Next, the substrate is relaxed to a flat configuration, and the tips are compressed together to form a macroscale contact. This break junction structure is introduced into a vacuum chamber and cooled to 4.2 K. To prepare an atomic-scale junction, the substrate is bent by a piezoelectric element (PI P-882 PICMA) that pushes the substrate at its center against two peripheral stoppers (Fig. 1c). As a result, the tips are pulled apart, and the contact cross-section is gradually reduced until a junction with a single-atom diameter neck is formed between the electrodes. Further extension leads to junction rupture. A fresh atomic junction can be prepared by relaxing the substrate, such that the electrode tips are pressed against each other to establish a multiatomic junction, after which the electrodes are pulled apart again to restore a single-atom junction. This break-make cycle can be iterated thousands of times such that the Ni electrode is wet by the softer metal of the counter electrode. After characterization of the bimetallic junction (Fig. S7a–c) to verify that the formed junction has now a typical conductance of a bare Cu, Ag, or Au junction as explained in ref. 52, the target molecules are introduced (See Supplementary Section 1 for details about the synthesis and characterization of the target molecules). We use a heated local molecular source to sublimate the target molecules into the cold junction, while repeating the break-make cycles. Once the typical conductance of the junction is altered (indicating the presence of molecules in the junction), the sublimation is stopped. Different molecular junctions are prepared by squeezing the electrodes to have a contact with a conductance of $\sim 20\ G_0$ followed by elongation of the contact up to rupture and the insertion of individual molecules between the electrodes. Repeating this procedure yields ensembles of molecular junctions with a variety of different geometries.

Conductance–displacement measurements

Conductance measurements as a function of elongation that provide the conductance histograms seen in Fig. S7 are done in the following way[52]. The junction is elongated at a rate of 20–40 Hz, while the conductance of the junction is measured simultaneously. The junction is biased with a fixed voltage provided by a DAQ card (NI-PCI6221) that is divided by 10 (by a homemade divider) to increase the signal-to-noise ratio. The resulting current across the junction is amplified by a current preamplifier (Femto amplifier DLPCA 200) and recorded by the DAQ card at a sampling rate of 50–200 kHz. The obtained current values are divided by the applied voltage values to extract the conductance. The interelectrode displacement is found by the exponential dependence of tunneling currents on the separation between the electrodes. The piezoelectric element that is used to bend the sample is driven by the same DAQ card connected to a piezo driver (Piezomechanik SVR 150/1).

Current–voltage measurements

The procedure for adjusting the junction before measuring current as a function of voltage (I–V measurement) is automated and based on the junction's stability over a specific time interval. A junction is formed by increasing the interelectrode distance until the conductance drops below the lowest conductance of the bare metal junction. At this point, the interelectrode distance is fixed, and the current is recorded for 1 s. If the conductance variations during this time interval remain below $1 \times 10^{-3}\ G_0$ ($G_0 \cong 1/12.9\ (\mathrm{k\Omega})^{-1}$ is the conductance quantum), an I–V measurement is conducted. However, if the conductance varies beyond $1 \times 10^{-3}\ G_0$ or the junction breaks during the measurement, the junction is reformed. Following this procedure, the junction is broken and reformed up to $\sim 20\ G_0$ to promote sampling of the span of junction structures. The I–V measurement itself is done as follows. Once a molecular junction is formed (typically within a conductance range of $1{\cdot}10^{-3}\ G_0$ and $8{\cdot}10^{-3}\ G_0$), a variable bias voltage is applied across the junction from the mentioned DAC card and divider. The voltage is swept at a rate of 0.5 V/s, while the current is measured as mentioned above. During repeated I–V measurements on different molecular junction realizations, a constant magnetic field is applied using a superconducting magnet (≤ 9 T) that provides a magnetic field parallel or antiparallel to the sample wire.

Magnetic field application

A superconducting solenoid (American Magnetics) applies a constant magnetic field. The studied break junction is located at the solenoid's center with its axis aligned to that of the solenoid. To avoid magnetostriction, we form hundreds of molecular junctions and perform the I–V measurements under a chosen fixed magnetic field. Before transitioning to the next measurement session at a different magnetic field, the interelectrode distance is increased to keep the junction broken while the magnetic field is altered to set a new fixed field. This procedure is done to avoid possible uncontrolled squeezing of the two electrodes against each other due to magnetostriction, which could otherwise modify the Ni(M) (M = Au, Ag, or Cu) electrode structure. The subsequent measurement session is thus conducted under a newly fixed magnetic field.

Data availability

Source data are provided as a Source Data file. Additional data are available from the corresponding author upon request. Source data are provided with this paper.

References

1. Ray, K., Ananthavel, S. P., Waldeck, D. H. & Naaman, R. Asymmetric scattering of polarized electrons by organized organic films of chiral molecules. *Science* **283**, 814–816 (1999).
2. Rikken, G. L. J. A., Fölling, J. & Wyder, P. Electrical magnetochiral anisotropy. *Phys. Rev. Lett.* **87**, 236602 (2001).
3. Krstić, V., Roth, S., Burghard, M., Kern, K. & Rikken, G. L. Magneto-chiral anisotropy in charge transport through single-walled carbon nanotubes. *J. Chem. Phys.* **117**, 11315–11319 (2002).
4. Rikken, G. L. J. A. & Wyder, P. Magnetoelectric anisotropy in diffusive transport. *Phys. Rev. Lett.* **94**, 016601 (2005).
5. Göhler, B. et al. Spin selectivity in electron transmission through self-assembled monolayers of double-stranded DNA. *Science* **331**, 894–897 (2011).
6. Xie, Z. et al. Spin specific electron conduction through DNA oligomers. *Nano Lett.* **11**, 4652–4655 (2011).
7. Pop, F., Auban-Senzier, P., Canadell, E., Rikken, G. L. J. A. & Avarvari, N. Electrical magnetochiral anisotropy in a bulk chiral molecular conductor. *Nat. Commun.* **5**, 3757 (2014).
8. Mtangi, W., Kiran, V., Fontanesi, C. & Naaman, R. Role of the electron spin polarization in water splitting. *J. Phys. Chem. Lett.* **6**, 4916–4922 (2015).
9. Aragonès, A. C. et al. Measuring the spin-polarization power of a single chiral molecule. *Small* **13**, 1602519 (2017).
10. Qin, F. et al. Superconductivity in a chiral nanotube. *Nat. Commun.* **8**, 14465 (2017).
11. Wakatsuki, R. et al. Nonreciprocal charge transport in noncentrosymmetric superconductors. *Sci. Adv.* **3**, e1602390 (2017).
12. Abendroth, J. M. et al. Analyzing spin selectivity in DNA-mediated charge transfer via fluorescence microscopy. *ACS Nano* **11**, 7516–7526 (2017).
13. Yokouchi, T. et al. Electrical magnetochiral effect induced by chiral spin fluctuations. *Nat. Commun.* **8**, 866 (2017).
14. Kettner, M. et al. Chirality-dependent electron spin filtering by molecular monolayers of helicenes. *J. Phys. Chem. Lett.* **9**, 2025–2030 (2018).

15. Al-Bustami, H. et al. Single nanoparticle magnetic spin memristor. *Small* **14**, 1801249 (2018).
16. Tokura, Y. & Nagaosa, N. Nonreciprocal responses from non-centrosymmetric quantum materials. *Nat. Commun.* **9**, 3740 (2018).
17. Aoki, R., Kousaka, T. & Togawa, Y. Anomalous nonreciprocal electrical transport on chiral magnetic order. *Phys. Rev. Lett.* **122**, 057206 (2019).
18. Rikken, G. L. & Avarvari, N. Strong electrical magnetochiral anisotropy in tellurium. *Phys. Rev. B.* **99**, 245153 (2019).
19. Lu, H. et al. Spin-dependent charge transport through 2D chiral hybrid lead-iodide perovskites. *Sci. Adv.* **5**, eaay0571 (2019).
20. Kulkarni, C. et al. Highly efficient and tunable filtering of electrons' spin by supramolecular chirality of nanofiber-based materials. *Adv. Mater.* **32**, 1904965 (2020).
21. Inui, A. et al. Chirality-induced spin-polarized state of a chiral crystal $CrNb_3S_6$. *Phys. Rev. Lett.* **124**, 166602 (2020).
22. Kim, Y.-H. et al. Chiral-induced spin selectivity enables a room-temperature spin light-emitting diode. *Science* **371**, 1129–1133 (2021).
23. Inui, A. et al. Chirality-induced spin polarization over macroscopic distances in chiral disilicide crystals. *Phys. Rev. Lett.* **127**, 126602 (2021).
24. Guo, C. et al. Switchable chiral transport in charge-ordered kagome metal CsV_3Sb_5. *Nature* **611**, 461–466 (2022).
25. Nakajima, R. et al. spin polarization and a pair of antiparallel spins in a chiral superconductor. *Nature* **613**, 479–484 (2023).
26. Yang, C. et al. Real-time monitoring of reaction stereochemistry through single-molecule observations of chirality-induced spin selectivity. *Nat. Chem.* **15**, 972 (2023).
27. Adhikari, Y. et al. Interplay of structural chirality, electron spin and topological orbital in chiral molecular spin valves. *Nat. Commun.* **14**, 5163 (2023).
28. Hannah, H. J. et al. Direct observation of chirality-induced spin selectivity in electron donor–acceptor molecules. *Science* **382**, 197–201 (2023).
29. Safari, M. R., Matthes, F., Schneider, C. M., Ernst, K. H. & Bürgler, D. E. Spin-selective electron transport through single chiral molecules. *Small*, **20** 2308233 (2023).
30. Liang, Y. et al. Enhancement of electrocatalytic oxygen evolution by chiral molecular functionalization of hybrid 2D electrodes. *Nat. Commun.* **13**, 3356 (2022).
31. Galperin, M. & Nitzan, A. Current-induced light emission and light-induced current in molecular-tunneling junctions. *Phys. Rev. Lett.* **95**, 206802 (2005).
32. Yeganeh, S., Ratner, M. A., Medina, E. & Mujica, V. Chiral electron transport: scattering through helical potentials. *J. Chem. Phys.* **131**, 014707 (2009).
33. Guo, A. M. & Sun, Q. Spin-selective transport of electrons in DNA double helix. *Phys. Rev. Lett.* **108**, 218102 (2012).
34. Gutierrez, R., Díaz, E., Naaman, R. & Cuniberti, G. Spin-selective transport through helical molecular systems. *Phys. Rev. B* **85**, 081404R (2012).
35. Gersten, J., Kaasbjerg, K. & Nitzan, A. Induced spin filtering in electron transmission through chiral molecular layers adsorbed on metals with strong spin-orbit coupling. *J. Chem. Phys.* **139**, 114111 (2013).
36. Maslyuk, V. V., Gutierrez, R., Dianat, A., Mujica, V. & Cuniberti, G. J. Enhanced magnetoresistance chiral molecular junctions.*Phys. Chem. Lett.* **9**, 5453–5459 (2018).
37. Yang, X., van der Wal, C. H. & van Wees, B. J. Spin-dependent electron transmission model for chiral molecules in mesoscopic devices. *Phys. Rev. B* **99**, 024418 (2019).
38. Michaeli, K. & Naaman, R. Origin of spin-dependent tunneling through chiral molecules. *J. Phys. Chem. C* **123**, 17043–17048 (2019).
39. Dalum, S. & Hedegård, P. Theory of chiral induced spin selectivity. *Nano Lett.* **19**, 5253–5259 (2019).
40. Fransson, J. Chirality-induced spin selectivity: the role of electron correlations. *J. Phys. Chem. Lett.* **10**, 7126–7132 (2019).
41. Zöllner, M. S., Saghatchi, A., Mujica, V. & Herrmann, C. Influence of electronic structure modeling and junction structure on first-principles chiral induced spin selectivity. *J. Chem. Theory Comput.* **16**, 7357–7371 (2020).
42. Liu, Y., Xiao, J., Koo, J. & Yan, B. Chirality-driven topological electronic structure of DNA-like materials. *Nat. Mater.* **20**, 638–644 (2021).
43. Alwan, S. & Dubi, Y. Spinterface origin chirality-induced spin-selectivity effect. *J. Am. Chem. Soc.* **143**, 14235 (2021).
44. Fransson, J. Charge and spin dynamics and enantioselectivity in chiral molecules. *J. Phys. Chem. Lett.* **13**, 808–814 (2022).
45. Evers, F. et al. Theory of chirality induced spin selectivity: progress and challenges. *Adv. Mater.* **34**, 2106629 (2022).
46. Wolf, Y., Liu, Y., Xiao, J., Park, N. & Yan, B. Unusual spin polarization in the chirality-induced spin selectivity. *ACS Nano* **16**, 18601 (2022).
47. Zhao, Y., Zhang, K., Xiao, J., Sun, K. & Yan, B. Magnetochiral charge pumping due to charge trapping and skin effect in chirality induced spin selectivity. *Nat. Commun.* **16**, 37 (2025).
48. Naskar, S., Mujica, V. & Herrmann, C. Chiral-induced spin selectivity and non-equilibrium spin accumulation in molecules and interfaces: a first-principles study. *J. Phys. Chem. Lett.* **14**, 694–701 (2023).
49. Rikken, G. L. J. A. & Avarvari, N. Comparing electrical magnetochiral anisotropy and chirality-induced spin selectivity. *J. Phys. Chem. Lett.* **14**, 9727–9731 (2023).
50. Dednam, W. et al. A group-theoretic approach to the origin of chirality-induced spin-selectivity in nonmagnetic molecular junctions. *ACS Nano* **17**, 6452–6465 (2023).
51. van Ruitenbeek, J. M., Korytár, R. & Evers, F. Chirality-controlled spin scattering through quantum interference. *J. Chem. Phys.* **159**, 024710 (2023).
52. Singh, A. K., Chakrabarti, S., Vilan, A., Smogunov, A. & Tal, O. Electrically controlled bimetallic junctions for atomic-scale electronics. *Nano Lett.* **23**, 7775–7781 (2023).
53. Yelin, T. et al. Conductance saturation in a series of highly transmitting molecular junctions. *Nat. Mater.* **15**, 444–449 (2016).
54. Barroso, J. et al. Revisiting the racemization mechanism of helicenes. *Chem. Commun.* **54**, 188–191 (2018).
55. Naaman, R., Paltiel, Y. & Waldeck, D. H. A perspective on chiral molecules and the spin selectivity effect. *J. Phys. Chem. Lett.* **11**, 3660 – 3666 (2020).
56. Ko, C. H. et al. Electron spin polarization and rectification driven by chiral perylene diimide-based nanodonuts. *J. Phys. Chem. Lett.* **14**, 10271–10277 (2023).
57. Yan, B. Structural Chirality and Electronic Chirality in Quantum Materials. *Annu. Rev. Mater. Res.* **54**, 97–115 (2024).
58. Kiran, V. et al. Helicenes—a new class of organic spin filter. *Adv. Mater.* **28**, 1957–1962 (2016).
59. Al-Bustami, H. et al. Atomic and molecular layer deposition of chiral thin films showing up to 99% spin selective transport. *Nano Lett.* **22**, 5022–5028 (2022).
60. Qian, Q. et al. Chiral molecular intercalation superlattices. *Nature* **606**, 902 (2022).
61. Giaconi, N. et al. Spin polarized current in chiral organic radical monolayers. *J. Mater. Chem. C.* **12**, 10029–10035 (2024).
62. Manchon, A. & Belabbes, A. Spin-orbitronics at transition metal interfaces. *Solid State Phys.* **68**, 1–89 (2017).
63. Liu, T. et al. Linear and nonlinear two-terminal spin-valve effect from chirality-induced spin selectivity. *ACS Nano* **14**, 15983–15991 (2020).
64. Hossain, M. A. et al. Transverse magnetoconductance in two-terminal chiral spin-selective devices. *Nanoscale Horiz.* **8**, 320–330 (2023).

Acknowledgements
We thank the following scientists (listed alphabetically) for fruitful discussions and comments: Y. Dubi, F. Evers, P. Hedegård, R. Korytár, L. Kronik, R. Naaman, A. Nitzan, G. L. J. A Rikken, S. Tirion, J. M. van Ruitenbeek, B. J. van Wees, L. Venkataraman, and B. Yan. This work was supported in France by the CNRS, the University of Angers, the RFI LUMOMAT and the French National Agency for Research (ANR) project SECRETS (ANR PRC 20-CE06-0023-01). O.T. acknowledges the support of the European Research Council (Grant 864008), the Israeli Science Foundation (Grant 2129/23), funding by the Harold Perlman family, and research grants from Dana and Yossie Hollander.

Author contributions
A.K.S., O.T., and N.A. designed the project. K.M., M.M.T., and A.H. performed the chemical synthesis, purification, and characterization of the compounds under the supervision of N.A. N.V. performed the chiral HPLC separation. A.K.S. fabricated the studied atomic and molecular junctions and conducted the experiments under the supervision of O.T. Experimental data analysis and model development were carried out by A.K.S., under the supervision of O.T. and N.A. A.K.S., N.A., and O.T. wrote the first draft with input from all other authors. A.K.S., N.A., and O.T. reviewed and edited the final draft.

Competing interests
The authors declare no competing interests.

Additional information
Supplementary information The online version contains supplementary material available at https://doi.org/10.1038/s41467-025-56718-9.

Correspondence and requests for materials should be addressed to Narcis Avarvari or Oren Tal.

Peer review information *Nature Communications* thanks Jan van Ruitenbeek, Peng Xiong, and the other, anonymous, reviewer(s) for their contribution to the peer review of this work. A peer review file is available.

Reprints and permissions information is available at http://www.nature.com/reprints

Publisher's note Springer Nature remains neutral with regard to jurisdictional claims in published maps and institutional affiliations.

Open Access This article is licensed under a Creative Commons Attribution-NonCommercial-NoDerivatives 4.0 International License, which permits any non-commercial use, sharing, distribution and reproduction in any medium or format, as long as you give appropriate credit to the original author(s) and the source, provide a link to the Creative Commons licence, and indicate if you modified the licensed material. You do not have permission under this licence to share adapted material derived from this article or parts of it. The images or other third party material in this article are included in the article's Creative Commons licence, unless indicated otherwise in a credit line to the material. If material is not included in the article's Creative Commons licence and your intended use is not permitted by statutory regulation or exceeds the permitted use, you will need to obtain permission directly from the copyright holder. To view a copy of this licence, visit http://creativecommons.org/licenses/by-nc-nd/4.0/.

© The Author(s) 2025

Supplementary Information for

Single-molecule junctions map the interplay between electrons and chirality

Anil-Kumar Singh[1], Kévin Martin[2], Maurizio Mastropasqua Talamo[2], Axel Houssin[2], Nicolas Vanthuyne[3], Narcis Avarvari[2*], and Oren Tal[1*]

[1]*Department of Chemical and Biological Physics, Weizmann Institute of Science, Rehovot 7610001, Israel*
[2]*Univ Angers, CNRS, MOLTECH-Anjou, SFR MATRIX, F-49000 Angers, France*
[3]*Aix Marseille Univ, CNRS, Centrale Marseille, UAR 1739, FSCM, Chiropole, Marseille, France*
[*] Corresponding authors

Content:

Section 1: Synthesis and characterization of the target molecule

Chemicals and instruments

All reagents and chemicals from commercial sources were used without further purification. Solvents were dried and purified using standard techniques. Column chromatography was performed with analytical-grade solvents using Aldrich silica gel (technical grade, pore size 60 *Å*, 230-400 mesh particle size). Flexible plates ALUGRAM® Xtra SIL G UV254 from MACHEREY-NAGEL were used for TLC. Compounds were detected by UV irradiation (Bioblock Scientific) or staining with iodine, unless otherwise stated.

NMR spectra were recorded with a Bruker AVANCE III 300 (^{1}H, 300 *MHz* and ^{13}C, 76 *MHz*) and Bruker AVANCE DRX 500 (^{1}H, 500 *MHz* and ^{13}C, 125 *MHz*). Chemical shifts are given in ppm relative to tetramethylsilane TMS and coupling constants *J* in *Hz*. Residual non-deuterated solvent was used as an internal standard.

Matrix Assisted Laser Desorption/Ionization was performed on MALDI-TOF MS BIFLEX III Bruker Daltonics spectrometer using dithranol, DCTB or α-terthiophene as matrix.

Synthetic procedures

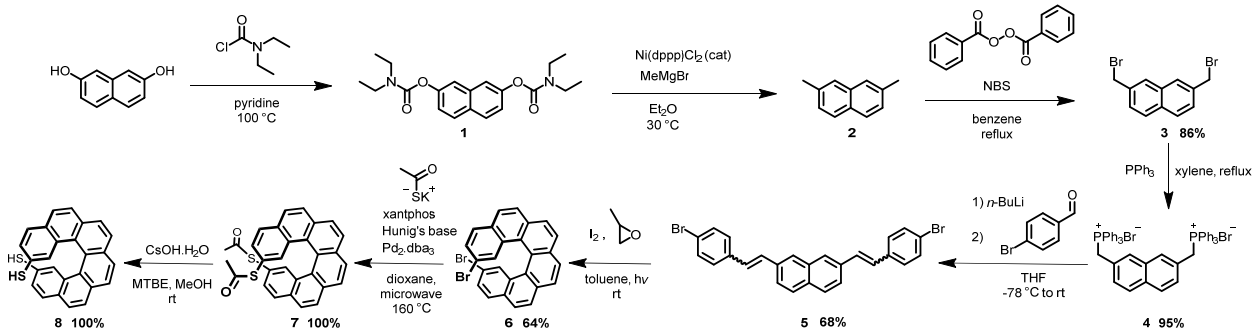

Fig. S1 | Synthetic pathway for the hexahelicene-2,15-dithiol 8. Multistep synthesis of the dithiole-[6]helicene **8** starting from 2,7-dihydroxy-naphthalene. The dibromo-[6]helicene intermediate **6** has been separated into its (P) and (M) enantiomers by chiral HPLC.

*naphthalene-2,7-diyl bis(diethylcarbamate) (**1**)*

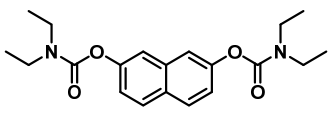

Compound **1** has been synthesized from 2,7-dihydroxy-naphthalene according to the published method (*1*).

*2,7-dimethylnaphthalene (**2**)*

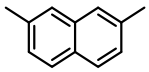

Compound **2** has been synthesized from **1** according to the published method[1].

*2,7-bis(bromomethyl)naphthalene (**3**)*

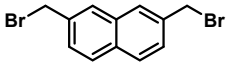

In a Schlenk tube under argon was dissolved **2** (780 mg, 3.22 mmol, 1 eq) in benzene (20 mL), then NBS (578 mg, 25.6 mmol, 1.1 eq) and benzoyl peroxide (105 mg, 0.64 mmol, 0.1 eq) were added in the dark. The mixture was stirred at reflux for 16 h; after reaching rt it was filtered off through a celite® pad. After purification *via* chromatography over silica gel column (PE/DCM, 9/1, Rf = 0.15), compound **3** was obtained as a white solid, 887 mg (86 % yield).

^{1}H NMR (300 *MHz*, Chloroform-*d*) δ 7.82 (d, *J* = 8.8 *Hz*, 4H), 7.52 (d, *J* = 9.8 *Hz*, 2H), 4.66 (s, 4H).

The spectral data for this compound match those reported in the literature[2].

*(naphthalene-2,7-diylbis(methylene))bis(triphenylphosphonium) bromide (**4**)*

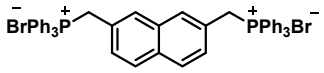

In a 100 *mL* flask was dissolved PPh_3 (5.51 *g*, 21.02 *mmol*, 3 *eq*) in xylene (57 *mL*), then **3** (2.2 g, 7.01 *mmol*, 1 *eq*) was added and the mixture was stirred at reflux for 20 h. After reaching the rt, the precipitate was filtered off and rinsed with cold Et_2O to afford (5.57 *g* (95 *%* yield) of **4** as a white powder.

^{1}H NMR (300 *MHz*, Chloroform-*d*) *δ* 7.86 – 7.57 (m, 30H), 7.48 (d, *J* = 8.3 Hz, 2H), 7.20 (s, 2H), 7.15 (d, *J* = 8.4 *Hz*, 2H), 5.53 (d, *J* = 14.3 *Hz*, 4H).

^{31}P NMR (122 *MHz*, Chloroform-d) *δ* 22.90.

The spectral data for this compound match those reported in the literature[3].

*2,7-bis(4-bromostyryl)naphthalene (**5**)*

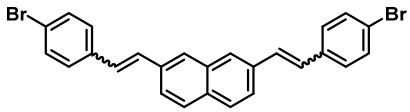

In a 250 *mL* Schlenk flask under argon was dissolved **4** (5 *g*, 5.96 *mmol*, 1 *eq*) in dry THF (100 *mL*). At -78 °C, *n*-BuLi (7.83 *mL*, 12.52 *mmol*, 1.6 M in hexane, 2.1 *eq*) was slowly added and the mixture turned from

white to red. After 15 min stirring, the mixture reached rt and stirred for 15 additional min. The mixture was then cooled down at -78 °*C* and p-bromobenzaldehyde (2.2 *g*, 11.92 *mmol*, 2 *eq*) was added. The mixture was stirred 15 *min* and turned to pale yellow and was then allowed to reach the rt and kept for 1 *h*. The crude product was filtered off through a celite® pad and rinsed with THF. After evaporation of the THF, the crude was purified via chromatography on silica gel column (petroleum ether/DCM, 9/1, Rf = 0.41 and 0.36). 2 g (68 *%* yield) of cis/trans of **5** were obtained as a beige powder.

^{1}H NMR (300 *MHz*, Chloroform-d) *δ* 7.79 – 7.69 (m, 2H), 7.68 – 7.57 (m, 3H), 7.53 – 7.39 (m, 2H), 7.34 (d, *J* = 8.4 *Hz*, 4H), 7.14 (dd, *J* = 8.7, 2.7 *Hz*, 5H), 6.77 (dd, *J* = 12.1, 8.3 *Hz*, 2H), 6.59 (dd, *J* = 12.1, 5.9 *Hz*, 2H).

The spectral data for this compound match those reported in the literature[4].

*11,14-dibromohexahelicene (**Br-[6]H-Br**) (**6**)*

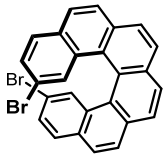

Stilbene **5** (0.25 *g*, 0.51 *mmol*, 1 *eq*) and iodine (8 *mg*, 0.03 *mmol*, 0.06 *eq*) were dissolved in toluene (650 *mL*) and THF (2 *mL*). The solution was bubbled with air for 15 *min*, and then was irradiated under stirring for 16 *h* with a Hg lamp (150 *W*). The synthesis was replicated in two batches, for a total amount of 1.2 *g* of stilbene compound. After evaporation of toluene, the crude was purified by chromatography over silica gel column (petroleum ether/DCM, 9/1, Rf = 0.56). 159 mg (64 *%* yield) of (*rac*)-**Br-[6]H-Br** were obtained as a light-yellow powder.

The spectral data for this compound match those reported in the literature[5].

The racemic compound was separated into its (M) and (P) enantiomers by chiral HPLC (vide infra).

*(P)-(S, S'-(hexahelicene-11,14-diyl)-diethanethioate) (**7**)*

Synthesized according to the following procedure[5].

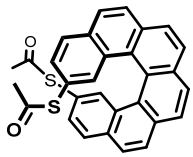

In a microwave flask under argon were dissolved (*P*)-**Br-[6]H-Br** (80 *mg*, 0.165 *mmol*, 1 eq), potassium thioacetate (56 *mg*, 0.49 *mmol*, 3 *eq*), xantphos (12 *mg*, 21 *µmol*, 0.13 eq) and $Pd_2.dba_3$ (9 *mg*, 10 *µmol*, 6 *mol%*) in dioxane (3.5 *mL*) followed by the addition of freshly distilled Hunig's base (0.1 *mL*, 0.6 *mmol*, 2 *eq*). After degassing with argon, the red solution was irradiated under microwave at 160 °*C* for 1 *h*. The organic layer was extracted with ethyl acetate, washed with water, dried over Na_2SO_4 and concentrated under vacuum. The crude oil was purified by chromatography over silica gel column (petroleum ether/EtOAc, 8/2, Rf = 0.6 and 0.3). 78 *mg* of (*P*)-**7** (quantitative yield) were obtained as a yellow solid.

7

^{1}H NMR (300 *MHz*, Chloroform-d) δ 8.07 – 7.93 (m, 10H), 7.88 (d, *J* = 8.3 *Hz*, 2H), 7.61 (d, *J* = 1.6 *Hz*, 2H), 2.15 (s, 6H).

^{13}C NMR (76 *MHz*, Chloroform-d) *δ* 194.40, 133.87, 133.53, 132.33, 131.91, 131.44, 129.88, 128.45, 127.94, 127.72, 127.66, 127.63, 127.26, 124.76, 30.01.

HRMS (m/z) [M^+] calcd. For $C_{26}H_{16}Br_2$, 476.0904; found 476.0895.

The preparation of the (M) enantiomer is identical, starting from (M)-**Br-[6]H-Br**.

*(P)-hexahelicene-2,15-dithiol (**8**)*

Synthesized according to the following procedure[6].

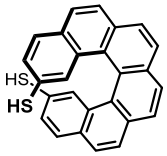

In a 100 *mL* flask under argon was dissolved (P)-**7** (40 *mg*, 0.084 *mmol*, 1 *eq*) in degassed MTBE (22 *mL*). Then a solution of $CsOH.H_2O$ (225.50 *mg*, 1.34 *mmol*, 16 *eq*) in degassed methanol (0.66 *mL*) was added dropwise and the mixture was stirred for 5 *min* at rt (the mixture turns yellow). Finally, was slowly added a solution of HCl (3.36 *mL*, 3.36 *mmol*, 1M, 40 *eq*) in H_2O (the mixture turns colorless). After extraction with MTBE, drying over Na_2SO_4 and concentration under vacuum, 32 *mg* (quantitative yield) of (P)-**8** were obtained as a yellow solid.

^{1}H NMR (300 *MHz*, Chloroform-d) *δ* 8.00 (d, *J* = 7.6 *Hz*, 4H), 7.89 (d, *J* = 0.6 *Hz*, 4H), 7.74 (d, *J* = 8.3 *Hz*, 2H), 7.54 (d, *J* = 1.8 *Hz*, 2H), 7.22 (dd, *J* = 8.3, 1.9 *Hz*, 2H), 2.87 (s, 2H).

^{13}C NMR (76 *MHz*, Chloroform-d) *δ* 135.93, 133.23, 132.05, 130.22, 130.19, 128.29, 127.58, 127.42, 127.39, 126.66, 126.25, 124.08.

HRMS (m/z) [M^+] calcd. For $C_{26}H_{16}S_2$, 392.0693; found 392.0691.

The preparation of the (M) enantiomer is identical, starting from (M)-**7**.

Chiral HPLC

Analytical chiral HPLC separation for compound **6**

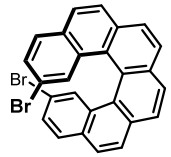

The sample is dissolved in dichloromethane, injected on the chiral column, and detected with an UV detector at 254 *nm*. The flow-rate is 1 *mL/min*.

Column	Mobile Phase	t1	k1	t2	k2	α	Rs
(*S*,*S*)-Whelk-O1	Heptane/dichloromethane 80/20	6.59	1.24	7.87	1.67	1.35	5.22

Table S1 | Analytical chiral HPLC separation conditions and characteristics for compound **6**.

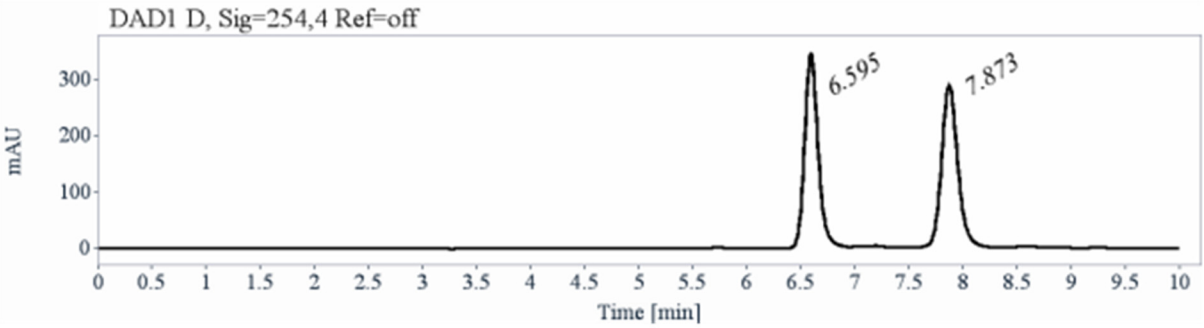

Fig. S2 | Analytical chiral HPLC for compound **6**.

RT [*min*]	Area	Area*%*	Capacity Factor	Enantioselectivity	Resolution (*USP*)
6.59	2964	49.91	1.24		
7.87	2974	50.09	1.67	1.35	5.22
Sum	5938	100.00			

Table S2 | Analytical chiral HPLC separation results for compound **6**.

Semi-preparative separation for compound **6**:

• Sample preparation: About 300 *mg* of compound **6** are dissolved in 60 *mL* of dichloromethane.

• Chromatographic conditions: (*S*,*S*)-Whelk-O1 (250 x 10 *mm*), hexane / dichloromethane (80/20) as mobile phase, flow-rate = 5 *mL/min*, UV detection at 350 *nm*.

• Injections (stacked): 335 times 180 *mL*, every 4.2 *min*.

• First fraction: 110 *mg* of the first eluted with ee > 99.5%

• Second fraction: 120 *mg* of the second eluted with ee >98 *%*

• Chromatograms of the collected fractions:

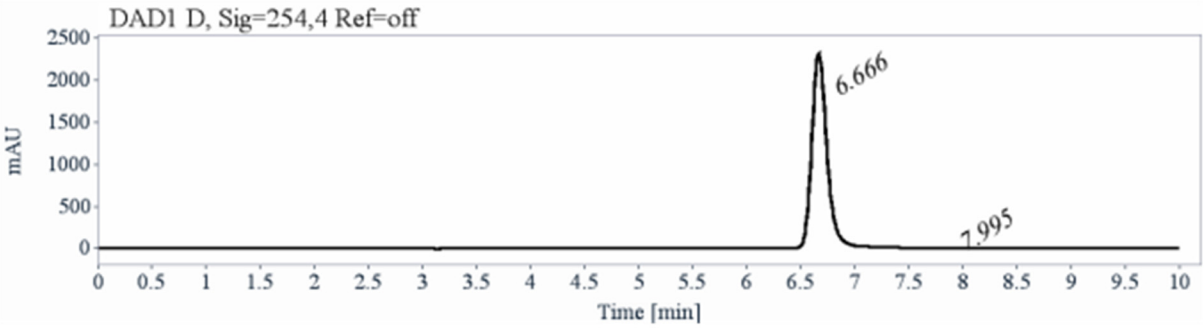

Fig. S3 | Chiral HPLC. Chiral semi-preparative HPLC separation for compound **6** first eluted.

RT [*min*]	Area	Area*%*
6.67	21990	99.98
7.99	4	0.02
Sum	21995	100.00

Table S3 | Semi-preparative chiral HPLC separation results for compound **6** first eluted enantiomer (P).

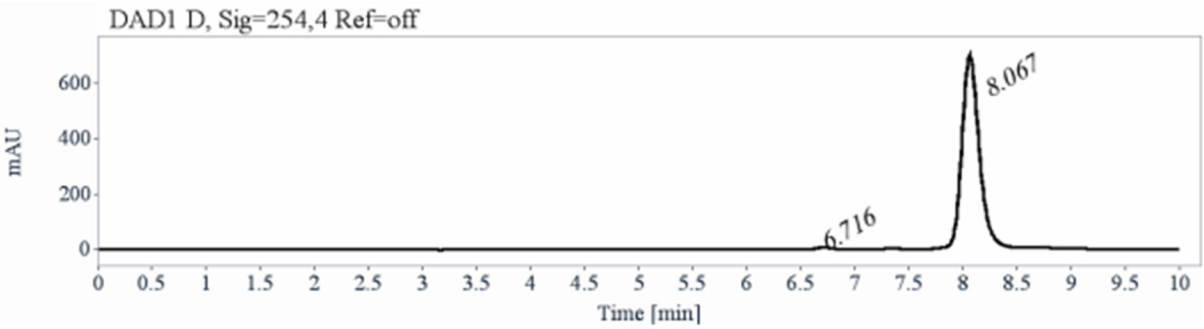

Fig. S4 | Chiral HPLC. Chiral semi-preparative HPLC separation for compound **6** second eluted.

RT [*min*]	Area	Area*%*
6.72	67	0.84
8.07	7848	99.16
Sum	7915	100.00

Table S4 | Semi-preparative chiral HPLC separation results for compound **6** second eluted enantiomer (M).

Optical rotations

Optical rotations were measured on a Jasco P-2000 polarimeter with a sodium lamp (589 *nm*), a halogen lamp (578, 546 and 436 *nm*), in a 10 *cm* cell, thermostated at 25*°C* with a Peltier controlled cell holder.

λ (*nm*)	**6** first eluted on (*S*,*S*)-Whelk-O1 $[\alpha]_\lambda^{25}$ (CH_2Cl_2, c =0.037)	**6** second eluted on (*S*,*S*)-Whelk-O1 $[\alpha]_\lambda^{25}$ (CH_2Cl_2, c =0.038)
589	+ 3500	- 3500
578	+ 3700	- 3700
546	+ 4600	- 4600
436	+ 13900	- 13900

Table S5 | Optical rotations for (P)-**6** (first eluted) and (M)-**6** (second eluted).

Electronic Circular Dichroism

ECD and UV spectra were measured on a JASCO J-815 spectrometer equipped with a JASCO Peltier cell holder PTC-423 to maintain the temperature at 25.0 ± 0.2*°C*. A CD quartz cell of 1 *mm* of optical pathlength was used. The CD spectrometer was purged with nitrogen before recording each spectrum, which was baseline subtracted.

The baseline was always measured for the same solvent and in the same cell as the samples.

The spectra are presented without smoothing and further data processing.

(P)-**6**, first eluted on (S,S)-Whelk-O1: green solid line, concentration = 0.158 *mmol.L*$^{-1}$ in dichloromethane.

(M)-**6**, second eluted on (S,S)-Whelk-O1: red dotted line, concentration = 0.153 *mmol.L*$^{-1}$ in dichloromethane.

Acquisition parameters: 0.1 nm as intervals, scanning speed 50 nm/min, band width 1 *nm*, and 1 accumulation per sample.

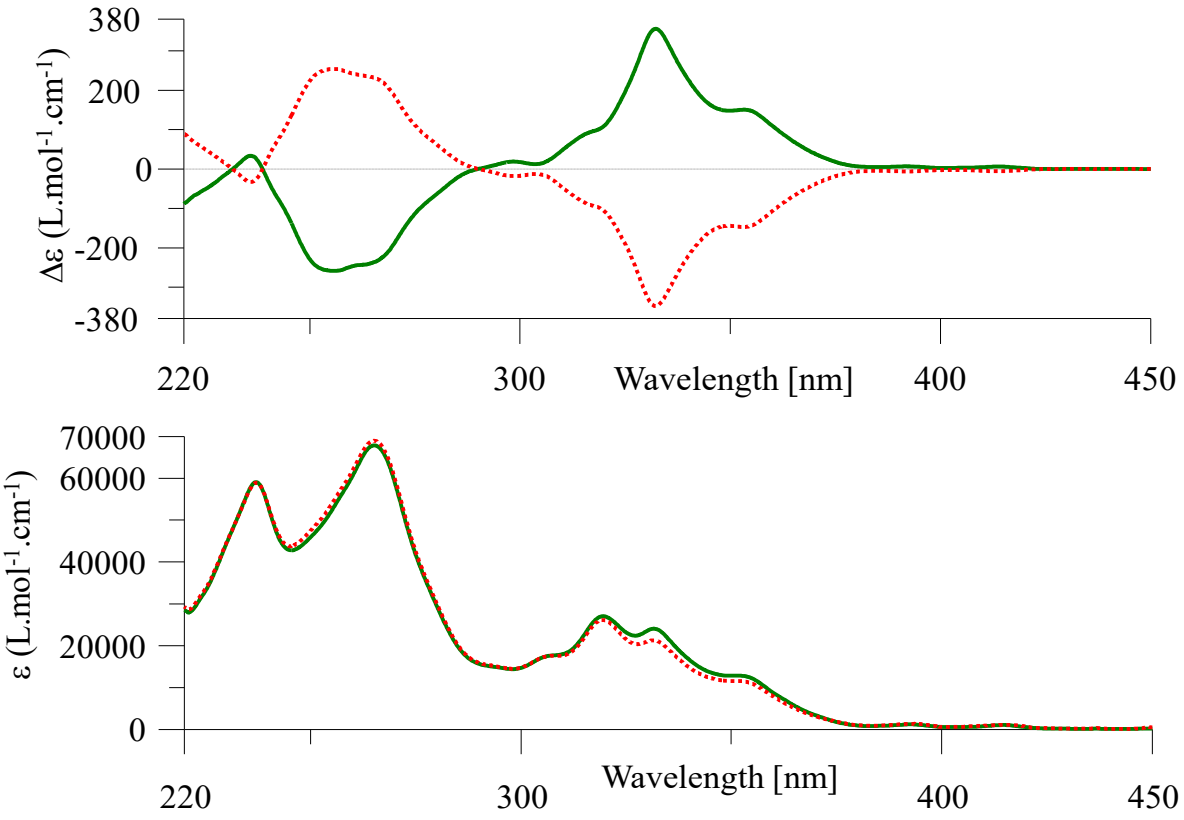

Fig. S5 | Spectroscopic characterization. CD (top) and UV-Vis (bottom) spectra of **6** first eluted (green line) and **6** second eluted (red dotted line).

ECD and UV spectra for **8** were measured on a JASCO J-1500 spectrometer. A CD quartz cell of 1 *cm* of optical pathlength was used. The CD spectrometer was purged with nitrogen before recording each spectrum, which was baseline subtracted. The baseline was always measured for the same solvent and in the same cell as the samples. The spectra are presented without smoothing and further data processing.

(P)-**8**: green solid line, concentration = 4.10^{-4} *mol.L*$^{-1}$ in chloroform.

(M)-**8**: red dotted line, concentration = $3.7.10^{-4}$ *mol.L*$^{-1}$ in chloroform.

Acquisition parameters: 0.5 *nm* as intervals, scanning speed 50 *nm/min*, band width 1 *nm*, and 1 accumulation per sample.

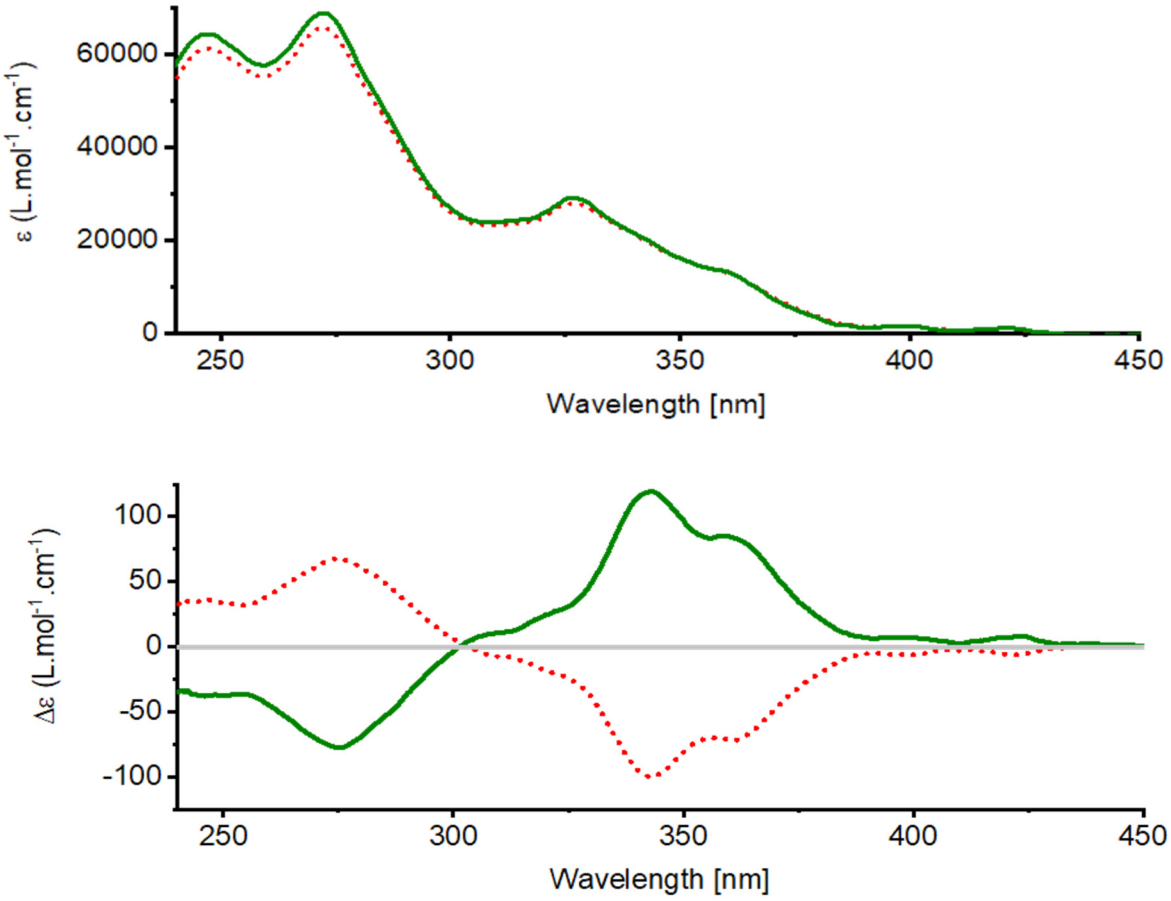

Fig. S6 | Spectroscopic characterization. CD (top) and UV-Vis (bottom) spectra of (P)-**8** (green line) and (M)-**8** (red dotted line).

Section 2: Electron transport measurements of the studied atomic and molecular junctions

Figures S7,a-c present conductance histograms based on repeated measurements (10,000) of conductance during junction elongation at 200 *mV* applied voltage for Cu-Cu, Ag-Ag, Au-Au metallic junctions, each with peaks identifies the most-probable conductance during junction stretching. For example, the dominant peak at ~1 G_0 represents the most probable conductance of a single atom contact[7-9]. As shown in ref. 10, when one metal electrode is made of a softer metal than the other, the softer metal wets the harder electrode tip, leading to metallic junctions with a constriction made of the

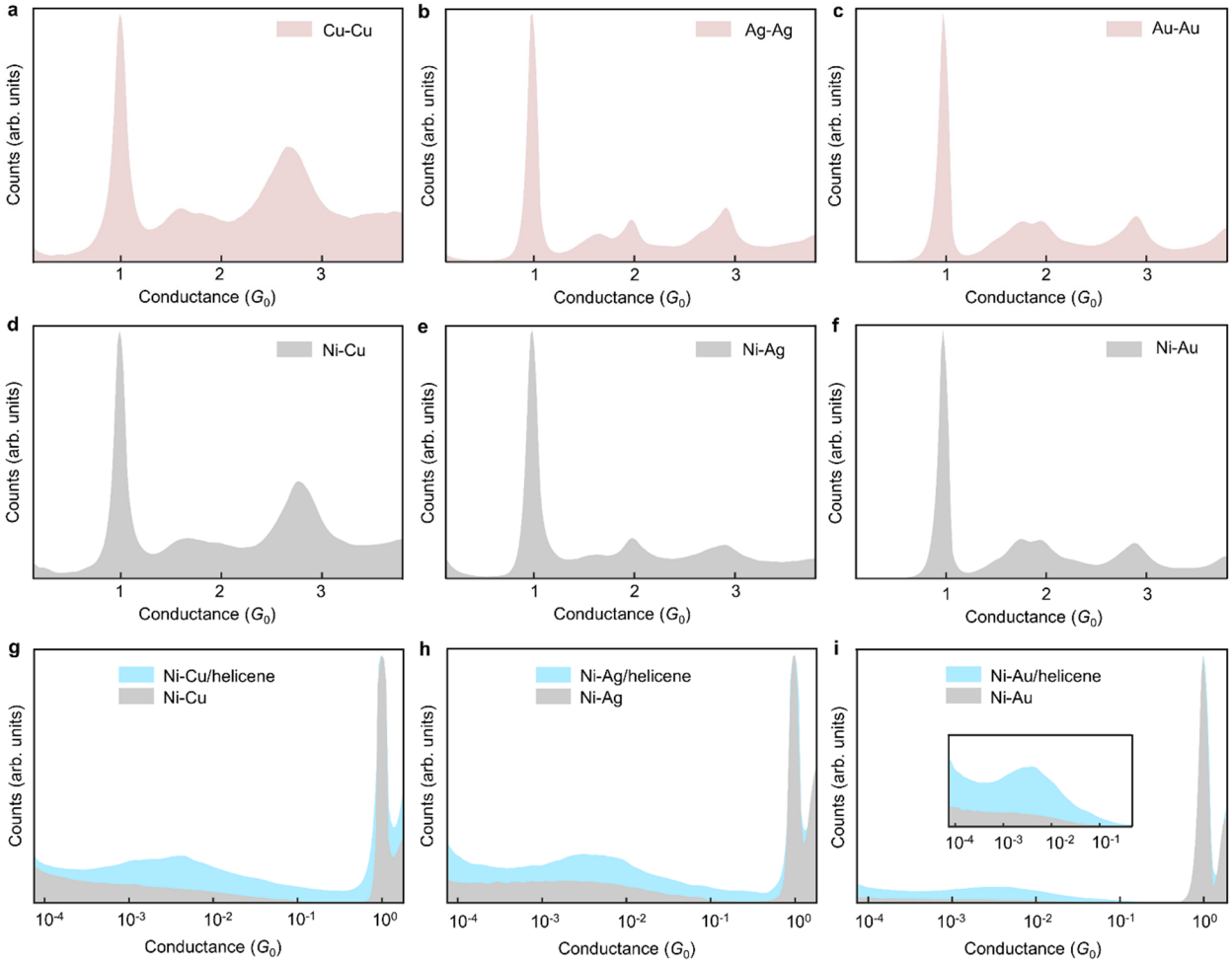

Fig. S7 | Conductance histograms for the considered atomic and molecular junctions. a-i, Conductance histograms at applied voltage of 200 mV for: Cu-Cu monometallic atomic junctions (a), Ag-Ag monometallic atomic junctions (b), Au-Au monometallic atomic junctions (c), Ni-Cu bimetallic atomic junctions (d), Ni-Ag bimetallic atomic junctions (e), Ni-Au bimetallic atomic junctions (f), Ni-Cu bimetallic atomic junctions in gray and Ni(Cu)-helicene-Cu molecular junctions in light blue (g), Ni-Ag bimetallic atomic junctions in gray and Ni(Ag)-helicene-Ag molecular junctions in light blue (h), and Ni-Au bimetallic atomic junctions in gray and Ni(Au)-helicene-Au molecular junctions in light blue (i). Inset of i: zoom-in image of the blue peak region.

soft metal. Similarly, in the studied cases here, the histograms for the Ni-Cu, Ni-Ag, and Ni-Au junctions presented in Fig. S7,d-e are essentially identical to the histograms taken for the Cu-Cu, Ag-Ag, and Au-Au junctions (Figs. S7, a-c), indicating that although the two macroscale electrodes are made of different metals, the atomic-scale constriction within the junctions that dominates their conductance is made of Cu, Ag, and Au respectively. Following the fabrication of metallic junctions with a repeated conductance of the softer metal, the target molecules were introduced. Figure S7,g-f show the conductance histograms of the formed molecular junctions after the introduction of the 2,2'-bis(thiol)-[6]helicene. In all three cases, the most probable conductance is centered between 10^{-3} G_0 to 10^{-2} G_0, allowing us to compare ensembles of I-V curves with a similar conductance for all the three cases.

Figure S8 presents the same data as in Fig. 1 in the main text, but in a polar presentation. Figure S9 shows individual *I-V* curves that were used to construct the average *I-V* curve and related histograms seen in

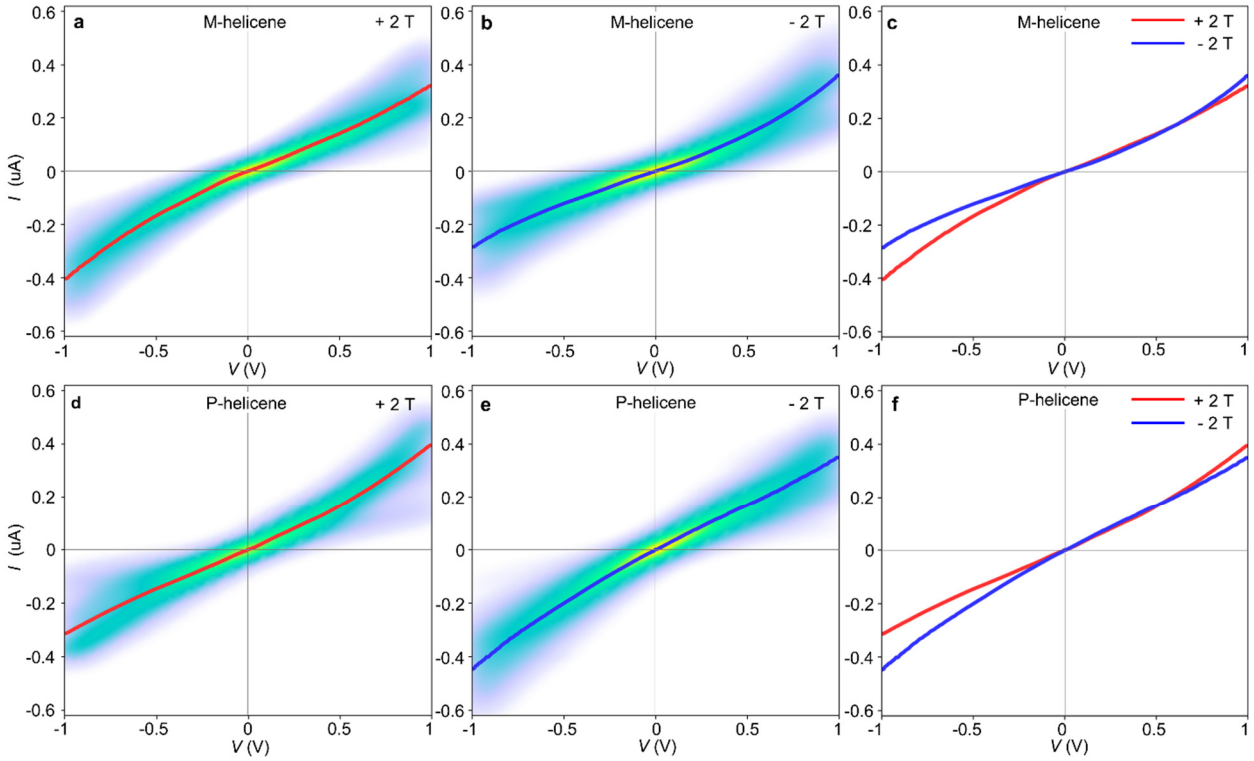

Fig. S8 | Polar presentation for current-voltage analysis of helicene molecular junctions under magnetic fields. **a**, Histogram and an average of current as a function of voltage (*I-V* curves) for Ni(Au)/M-helicene/Au junctions under +2 **T** magnetic field, parallel to the junction. **b,** The same under -2 **T** magnetic field antiparallel to the junction. **c,** Average current as a function of voltage for Ni(Au)/M-helicene/Au junctions under parallel and antiparallel +2 **T** and -2 **T** magnetic fields. **d-f**, The same as (a-c) but for Ni(Au)/P-helicene/Au junctions. The number of examined molecular junctions in each case varies between 251 to 377.

Fig. 1. To facilitate the observation of individual I-V curves in Fig. S9, we present every 10th curve out of the ensembles used in constructing Fig. 1 and Fig. S8. Importantly, across all the measured individual *I-V* curves, we never observed an asymmetry opposite to that demonstrated by the average curves, for a given chirality and magnetic field.

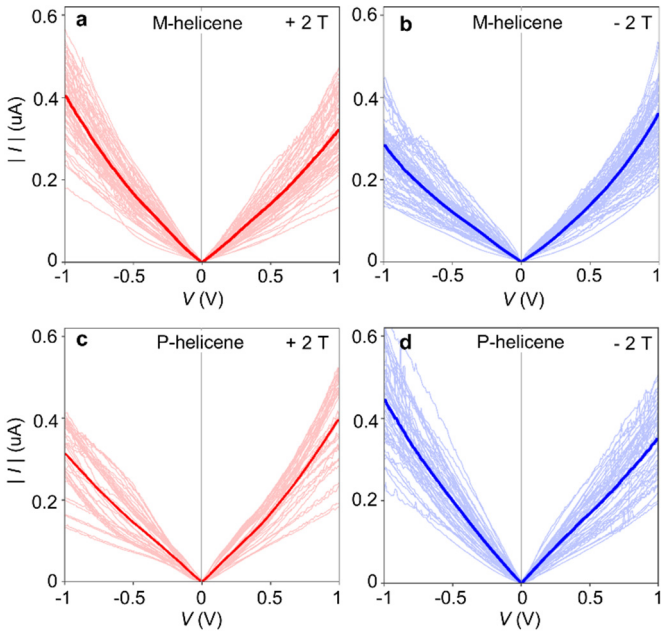

Fig. S9 | Individual *I-V* curves for the two enantiomers and magnetic field orientations. a, *I-V* curves for Ni(Au)/M-helicene/Au junctions under +2 **T** magnetic field, parallel to the junction. **b,** The same under -2 **T** magnetic field antiparallel to the junction. **c-d**, The same as (a-b) but for Ni(Au)/P-helicene/Au junctions. The thick curves represent the average *I-V* curves for the entire ensembles used in Fig. 1 and Fig. S7. Here, we present every 10th curve out of the mentioned ensembles to allow the observation of individual curves.

Figure S10 presents the standard error of the average *I-V* curves shown in Fig. 1f and i, as well as the average itself, displayed as a thinner line compared to Fig. 1. This format is not used in the main text due to the reduced figure size, which would render the details unclear.

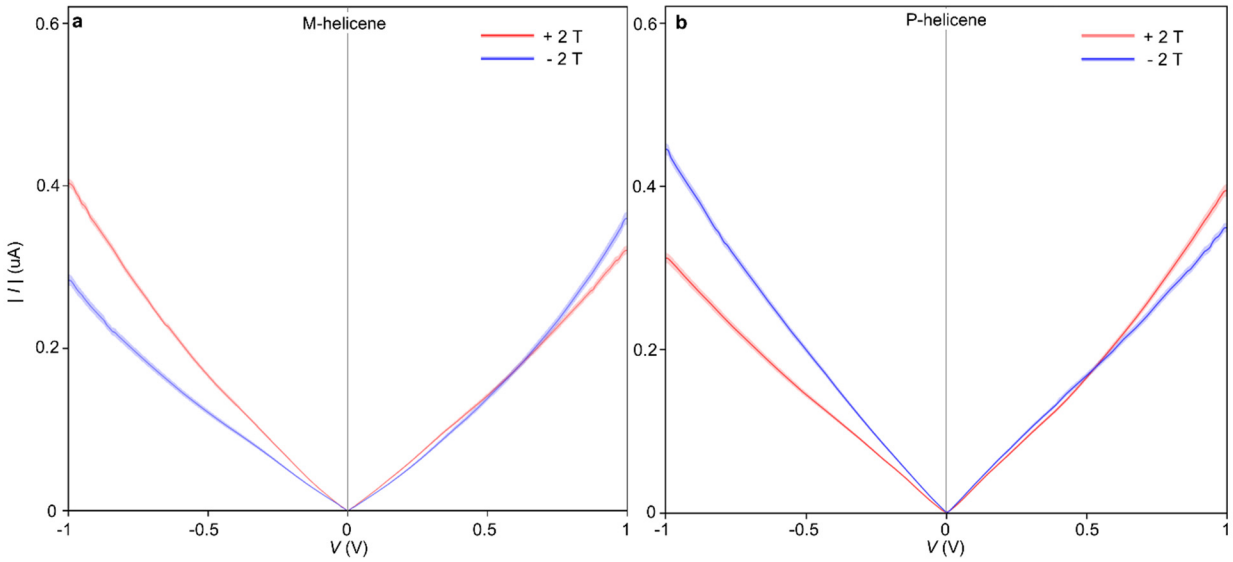

Fig. S10 | Average *I-V* curves and standard error for the data presented in Fig. 1. a, Average *I-V* curves (solid lines) and standard error (shaded areas) for Ni(Au)/M-helicene/Au junctions under +2 **T** (red) and -2 **T** (blue). **b,** The same for Ni(Au)/P-helicene/Au junctions.

According to Fig. S7 the range of the most probable conductance during elongation of the examined molecular junctions is roughly 10^{-2}-10^{-3} G_0. This values were measured at an applied voltage of 200 *mV*. In Fig. 1 the span of the current at 200 *mV* exhibits a similar range of one order of magnitude. This is seen by the cross-section of Fig. 1a at 200 *mV*, shown in Fig. S11a, including the average current. Relying on the rather linear I-V curve in the relevant voltage range, we can divide the current by 200 *mV* to obtain the counts versus dc conductance range at 200 *mV*. This is shown in Fig. S11b together with the average conductance. Here, the range of the obtained conductance is $1{\cdot}10^{-3}$ - $8{\cdot}10^{-3}$ G_0, which agrees with the above mentioned 10^{-2}-10^{-3} G_0 range.

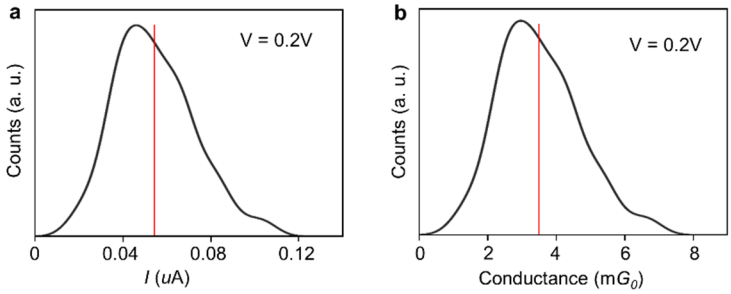

Fig. S11 | Current and conductance distributions for the data presented in Fig. 1 at a voltage of 200 *mV*. a, Current histogram showing a cross section of Fig. 1 at 200 *mV*. The red line indicates the average current. **b,** Conductance histogram obtained by dividing the current values in (a) by 200 *mV*. The red line represents the average conductance.

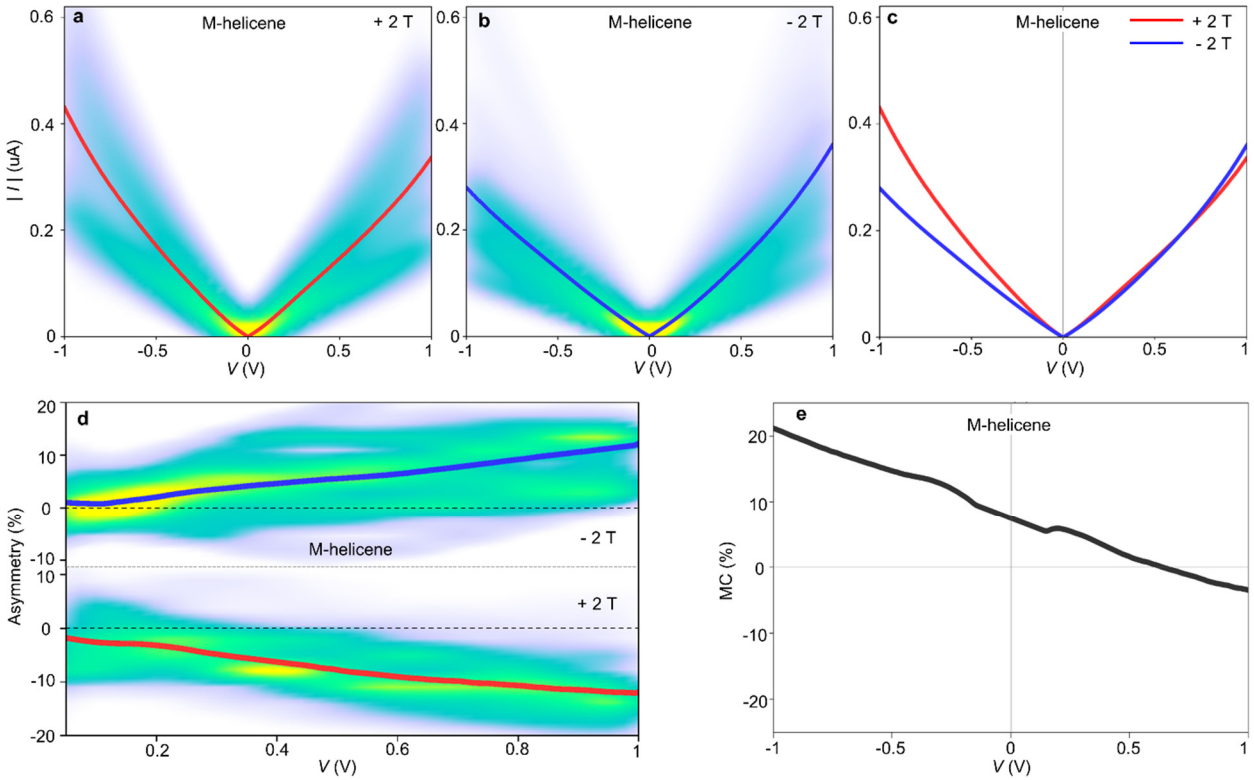

Fig. S12 | Similar analysis as in Fig. 1 and MC for Ni(Au)/M-helicene/Au junctions obtained using a different sample. **a,** Histogram and an average of $|I|$-V curves under +2 **T** magnetic field, parallel to the junction. **b,** The same under -2 **T** magnetic field antiparallel to the junction. **c,** Average $|I|$-V curves under parallel and antiparallel +2 **T** and -2 **T** magnetic fields. The standard error of the current $[(\text{standard deviation})/\sqrt{\#\text{ of curves}}]$ is smaller than the curve width. **d,** Asymmetry (defined in the main text) as a function of voltage magnitude under the mentioned opposite magnetic fields. **e,** Average MC (defined in the main text) based on the average *I*-*V* curves from (c), above ± 100 *mV*. The number of examined molecular junctions (and corresponding *I*-*V* curves) is 671 for +2 **T** and 573 for -2 **T**.

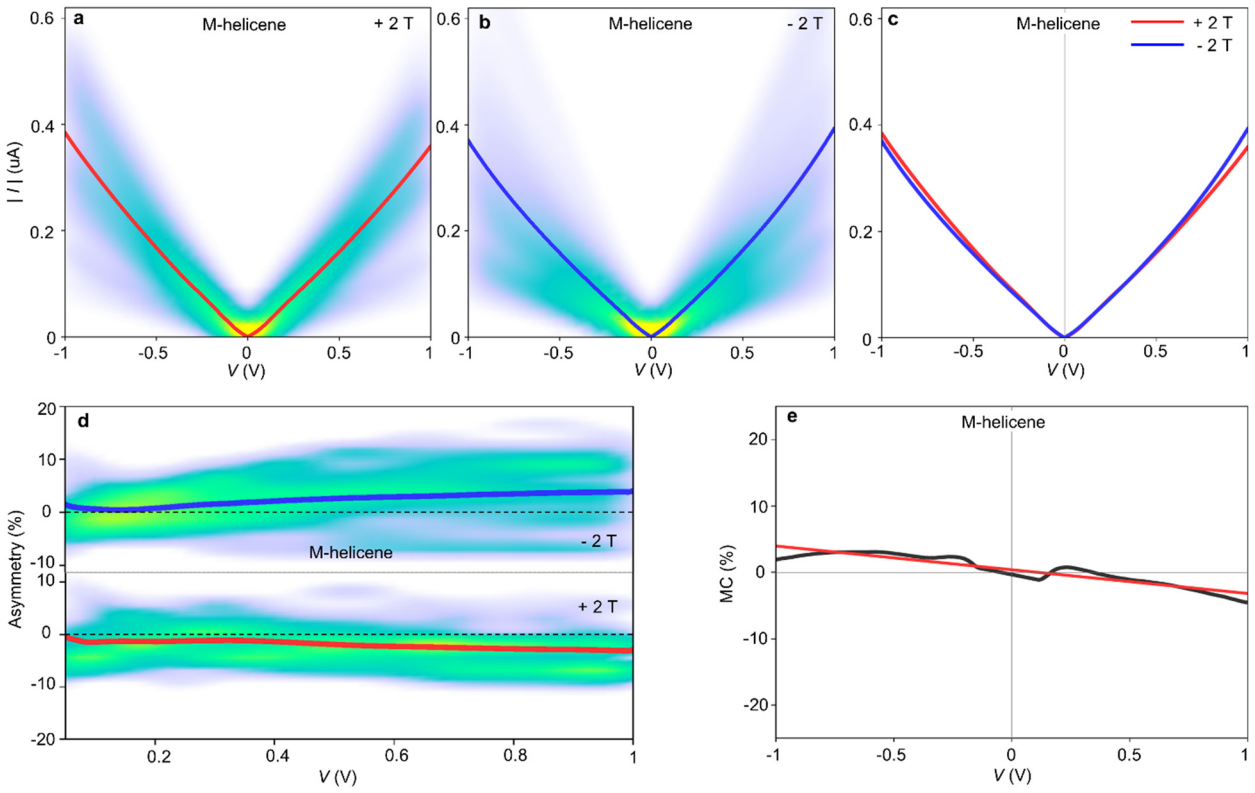

Fig. S13 | *I-V* curves under magnetic fields, asymmetry, and MC for Au/M-helicene/Au junctions. a, Histogram and an average of $|I|$-*V* curves under +2 **T** magnetic field, parallel to the junction. **b,** The same under -2 **T** magnetic field antiparallel to the junction. **c,** Average $|I|$-*V* curves under parallel and antiparallel +2 **T** and -2 **T** magnetic fields. The standard error of the current is smaller than the curve width. **d,** Asymmetry as a function of voltage magnitude under the mentioned opposite magnetic fields. Asymmetry is defined in the main text **e,** Average MC (black) based on the average *I-V* curves from (c), above $\pm$100 *mV* for robust results. The green curve represents a fit to the black measured curve. The number of examined molecular junctions (and corresponding *I-V* curves) is 685 for +2 **T** and 845 for -2 **T**.

Section 3: Complementary data to Fig. 2.

Generation of the I-V curves presented in Figs. 2b and c:

In figs. 2b and c, we present general *I-V* characteristics that are aligned with the behavior observed for the CISS and EMCA effects in previous studies[11-20]. Specifically, we adapted the following approach. For a given molecule's chirality, the total current I' can be expressed as a combination of the intact current I, as well as the CISS and EMCA terms, as follows:

$$I' = I + \alpha_i^c I + \beta^c (I \cdot B)V$$

where $I = AV + DV^3$ for a tunneling junction[21]. The constants A and D are determined by the junction's conductance. The constant α_i^c (here, $i = \uparrow, \downarrow$ - electron's spin orientation ; c - chirality) represents the strength of the CISS effect for a given chiral conductor, where its sign depends on the electron's spin orientation, i (parallel or antiparallel to the conductor), and the conductor's chirality. The term $\alpha_i^c I$ effectively reproduces the previously observed general I-V behavior related to the CISS effect. The last term, $\beta^c (I \cdot B)V$, describes the EMCA effect. It relies on both the current I and the magnetic field B[22]. The constant β^c signifies the strength of the EMCA effect for a given chiral conductor, and its sign depends on the molecule's chirality.

For the *M*-enantiomer, Figs. 2,b and c illustrates the I-V curves attributed to the CISS and EMCA effects, respectively. In a parallel magnetic field orientation (B>0) and a positive voltage, the CISS term induces a positive correction to the current (see red curve in Fig. 2b), whereas for the same magnetic field and voltage conditions, the EMCA term elicits a negative correction (see red curve in Fig. 2c). The former is attributed to the prevalence of spins oriented antiparallel to the junction's axis when the Nickel electrode's magnetization is parallel, as a result of a dominant minority spin population at the Fermi energy. In contrast, for a negative voltage and a parallel magnetic field, both terms contribute positively, leading to an enhanced current magnitude for the red curves. The situation is inverted for an antiparallel magnetic field orientation (B<0), as seen for the blue curves in Figs. 2b and c. To correctly describe the contributions of the CISS and EMCA effects for the *P*-enantiomer, the signs of α_i^c and β^c should be inverted.

The green curves in Figs. 2f and g are linear fits to the symmetric and antisymmetric MC components obtained from the experiment, ignoring fine details that may be ascribed to the local junction's electronic structure. However, these linear curves can also be produced by the above equation with A, D, α_i^c, and β^c as adjustable parameters. Specifically, using the above equation and the MC definition a linear curve identical to the linear fit to the experimental results in Fig. 2e is found by adjusting the parameters. Then,

the intercept with the MC axis yields a linear MC function identical to the fit in Fig. 2f and the slope is used to construct identical linear function to the fit in Fig. 2g. The values of A, D, α_i^c, and β^cB (for B=+2 **T** or -2 **T**) that are found in these fit procedure, are then used to construct the *I-V* curves presented in Figs. 2,b and c, where A and D are identical to both figures, α_i^c is used to produce Fig. 2b and β^cB is used to construct Fig. 2c. Remarkably, we only changed the signs of α_i^c and β^c, which were extracted by the fit to the experimental MC data for the M-helicene junctions (Fig. 2e) to obtain the linear green curve in Fig. 2h that fits very well the experimental MC data (black), found for P-helicene junctions in independent experiments.

The used values for the fitting parameters are A=1·10^{-7} $\mu Amp/V$, D=3·10^{-7} $\mu Amp/V^3$. For the M-enantiomer and a parallel magnetic field (+2 **T**), we used α_i^c= 0.078, and β^c= -0.0625 $T^{-1}V^{-1}$. For the M-enantiomer and an antiparallel magnetic field (-2 **T**), we used the same α_i^c magnitudes but with the opposite sign, while β^c remains unchanged (though β^cB changes sign due to the change in B sign). For junctions based on the P-helicene, Figs. S14a and b present the symmetric (a) and antisymmetric (b) MC components of the

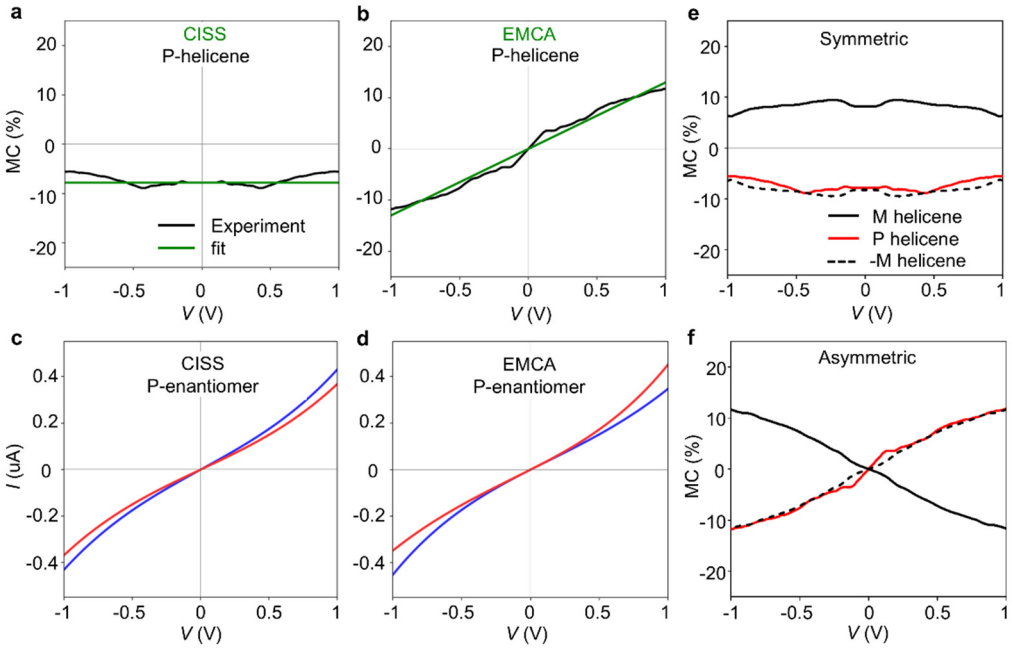

Fig. S14 | Expected *I-V* curves and MC considering the CISS and EMCA effects. a,b, Symmetric (a) and antisymmetric (b) components of the measured MC for Ni(Au)/P-helicene/Au junctions (black) and linear functions (green) calculated as explained in the text. **c,d,** Simulated *I-V* curves for the CISS effect (a), and EMCA effect (b), considering *P*-enantiomer junctions. Red curves represent the *I-V* response under a parallel (positive) magnetic field and blue curves represent the response under an antiparallel (negative) magnetic field. Using the MC definitions, the curves in (c,d) provide the green curves in (a,b), respectively. **e,f,** Symmetric (e) and antisymmetric (f) components for measured MC for P- and M-helicene junctions. The M-helicene curves were generated by inverting the signs of the data obtained for the M-enantiomer junctions. Details of the calculations are provided in the text.

overall MC presented in Fig. 2h. To generate the green curves in S13a and b, we simply took the opposite signs for the above mentioned α_i^c and β^c values used for the M-enantiomer junctions, while keeping the A and D parameters the same and used the MC definition. The sum of these MC curves provides the green curve in Fig. 2h, and the obtained *I-V* curves using these four parameters are presented in Figs. S14c and d. Interestingly, Figs. S14e shows that inverting the symmetric component of the experimentally obtained MC for M-helicene junctions results in an excellent match with the symmetric MC component for the P-helicene junctions. Similarly, Fig. S14f demonstrates this for the antisymmetric MC component.

Note that the mentioned equation describes the general trend of the measured *I-V* curves. However, this work does not focus on the behavior of the CISS and EMCA effects when the applied voltage approaches zero since MC is examined only above $\pm 100\,mV$ for Au-based junctions. Thus, we cannot conclude whether the CISS contribution behaves differently than $\alpha_i^c I(V)$ under these conditions.

MC nullification:

The origin for the MC nullification in Figs. 2e and h comes from the different influence of the CISS and EMCA on the current. This is illustrated by the I-V curves in Fig. 2b and c, attributed to the CISS and EMCA effects, respectively. At a positive magnetic field, the CISS effect leads to current magnitude enhancement (Fig. 2b, red curve) at both voltage polarities. However, at a positive magnetic field the EMCA suppresses the current magnitude at a positive voltage and enhances it at a negative voltage (Fig. 2c, red curve). As a result, the influence of the two effects on the current adds up at a negative voltage and oppose each other at a positive voltage. At a certain positive voltage the enhancement of the current by the CISS effect exactly cancels the suppression of the current by the EMCA effect. This is translated to *I-V* crossing in Fig. 2a and MC nullification in Fig. 2e at a positive voltage. The MC nullification is a universal feature in the sense that the same measurement for the opposite conductor's chirality result *I-V* crossing and MC nullification at the same voltage. This can be seen by the experimental *I-V* and MC data for the M-helicene (Figs. 2a and e) and P-helicene (Figs. 2d and h) junctions. Focusing on the *I-V* curves in Fig. 2a and d, the larger separation between the blue and red curves at negative voltages and the smaller separation at positive voltages arise from the same effect: CISS and EMCA add up at negative voltages but cancel each other at positive voltages.

Section 4: The relation between asymmetry and conductance difference.

We define asymmetry as:

$Asymmetry = 100 \cdot [|I(+V)| - |I(-V)|]/[|I(+V)| + |I(-V)|]$

Dividing the numerator and denominator by V, where: $V = |(+V)| = |(-V)|$ is the voltage magnitude for the same positive and negative voltage, $(+V) = -(-V)$,

we get: $Asymmetry = 100 \cdot [|I(+V)|/V - |I(-V)|/V]/[|I(+V)|/V + |I(-V)|/V]$

For: $G(+V) = |I(+V)|/V$, and $G(-V) = |I(-V)|/V$,

we have: $Asymmetry = 100 \cdot [|G(+V)| - |G(-V)|]/[|G(+V)| + |G(-V)|]$

Since the conductance difference is defines as: $\Delta G(V) = |G(+V)| - |G(-V)|$,

we get: $Asymmetry = 100 \cdot [\Delta G(V)/[|G(+V)| + |G(-V)|]$

Namely, the asymmetry is proportional to the conductance difference, for a given voltage magnitude.

Section 5: Magnetoconductance shift extracted by linear fitting

In the analysis presented in Fig. S15, we ignore the fine structure of the MC curves and use a linear fit to evaluate the MC shift at zero voltage in order to have a quantity that is not solely determined by the specific MC obtained at zero voltage. The data presented in Fig. S15b and Fig. S15c correspond to Fig. 3k and Fig. 4k, respectively, but with R-square values.

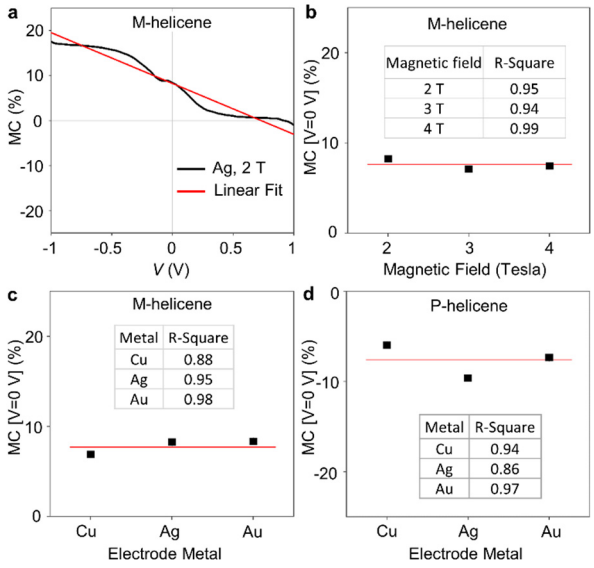

Fig. S15 | **Magnetoconductance shift analysis based on linear fits. a,** Example of a linear fit (red) to a MC curve (black). **b**, MC shift based on the linear fit value at zero voltage as a function of magnetic field magnitudes for junctions based on M-helicene. **c**, MC shift based on the linear fit value at zero voltage as a function of the counter electrode metal type for junctions based on *M*-helicene. **d,** The same as (c) for junctions based on P-helicene. Error bars are smaller than the symbols. The R-Square of each fit is presented in the inset tables.

Section 6: The influence of the metal on the CISS effect

For a sufficiently thick layer of the nonferromagnetic metal (Au, Ag, Cu) on the Ni tip, the spin polarization of the injected current experienced by the molecule is expected to be strongest for Cu based junctions and weakest for Au based junctions, due to their different spin diffusion lengths. This would translate to a small MC shift for Au-based junctions, an intermediate MC shift for Ag-based junctions and a large MC shift for Cu-based junctions. The fact that we clearly do not observe this trend in Fig. 4k suggests that either the effect is negligible, or it is canceled out by opposing effect(s).

In previous simulations for Ni and Au[23,24], when a Ni tip is indented into Au, the wetting layer consists of only 1-3 atomic layers of Au on the Ni tip, with a thickness of several Angstroms. In our experiments, we indent the tips to a similar extent or less than in these simulations (up to conductance of 20 G_0). For Ag and Cu, we expect a similar effect, although Ni-nonferromagnet indentation has not been studied for these two metals.

A rough estimate of the necessary nonferromagnet thickness to produce a non-negligible effect on the injected spin population can be derived from the spin diffusion lengths, which are presented in Table S6 for the three metals at relevant temperatures. As shown, the spin diffusion length for Au is more than an order of magnitude larger than the expected thickness of an Au wetting layer on the Ni tip. For Ag and Cu, even if we assume for some reason a somewhat thicker wetting layer on the Ni tip, their spin diffusion lengths are larger than that of Au, suggesting a negligible effect on spin injection also for Ag and Cu based junctions. Therefore, in our experiments, this effect is expected to be negligible.

Metal	Reference	Temperature	Spin diffusion length
Au	25	4.5*K*	35 *nm* +65 *nm*/-20 *nm*
	26	10*K*	33 ± 9 *nm*
Ag	27	4.2*K*	>40 *nm*
	28	10*K*	127-851 *nm*
Cu	29	4.2*K*	1000 *nm*
	30	4.2*K*	1000 *nm*
	31	4.2*K*	546 *nm*

Table S6 | Spin diffusion length for Au, Ag and Cu at relevant temperatures based on former studies.

Note that the expected Au thickness was estimated based on earlier calculations, and we do not have direct experimental measurements to support this estimation. While we cannot exclude the possibility of a finite influence of the Au wetting layer on spin dephasing, we expect this effect to be negligible given the estimated Au thickness and the averaging out of contributions from potential peculiar Au structures on the Ni electrode

Section 7: Additional complementary figures

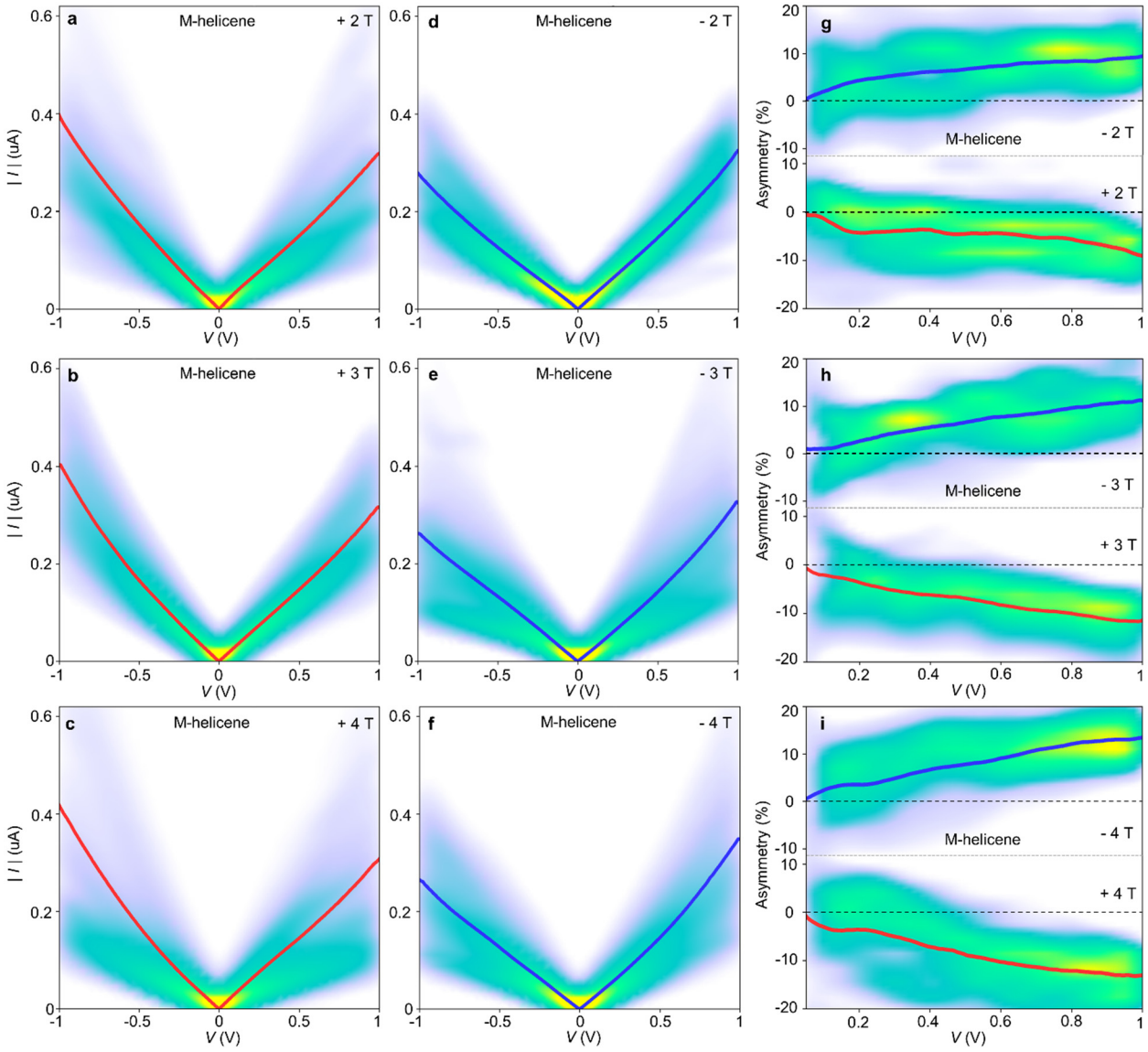

Fig. S16 | **Current as a function of voltage and asymmetry histograms at different magnetic fields. a-f,** Histogram and an average of current in absolute values as a function of voltage for Ni(Ag)/M-helicene/Ag junctions at different applied magnetic fields. **g-l,** Histogram and an average Asymmetry as a function of applied voltage magnitude at different applied magnetic fields. The number of examined molecular junctions in each case varies between 372 to 634.

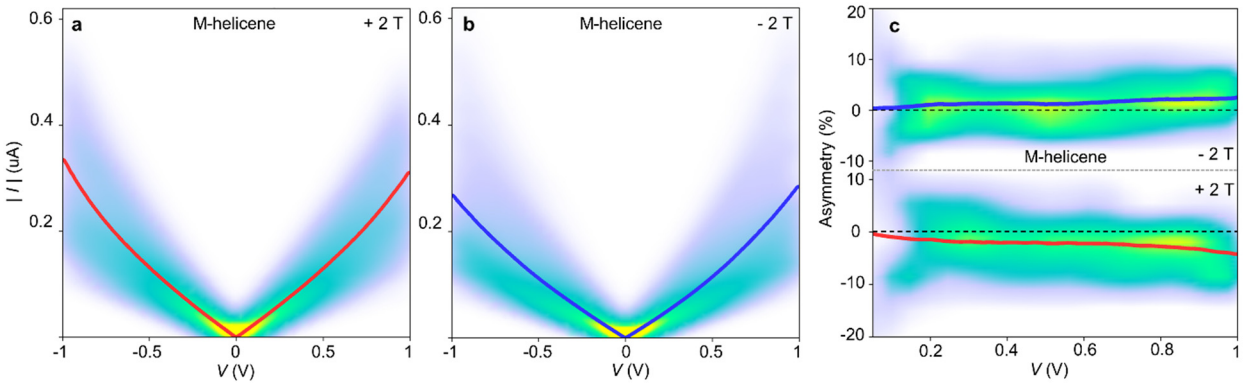

Fig. S17 | **Current as a function of voltage and asymmetry histograms for Cu based junctions. a**,**b**, Histogram and an average of current in absolute values as a function of voltage for Ni(Cu)/M-helicene/Cu junctions at parallel and antiparallel magnetic field orientations. **c**, Histogram and an average Asymmetry as a function of applied voltage magnitude. Measurements were done at an applied magnetic field of +2 **T** or -2 **T**. The standard error of the current is smaller than the curve width. The number of examined molecular junctions is 416 for +2 **T** and 443 for -2 **T**.

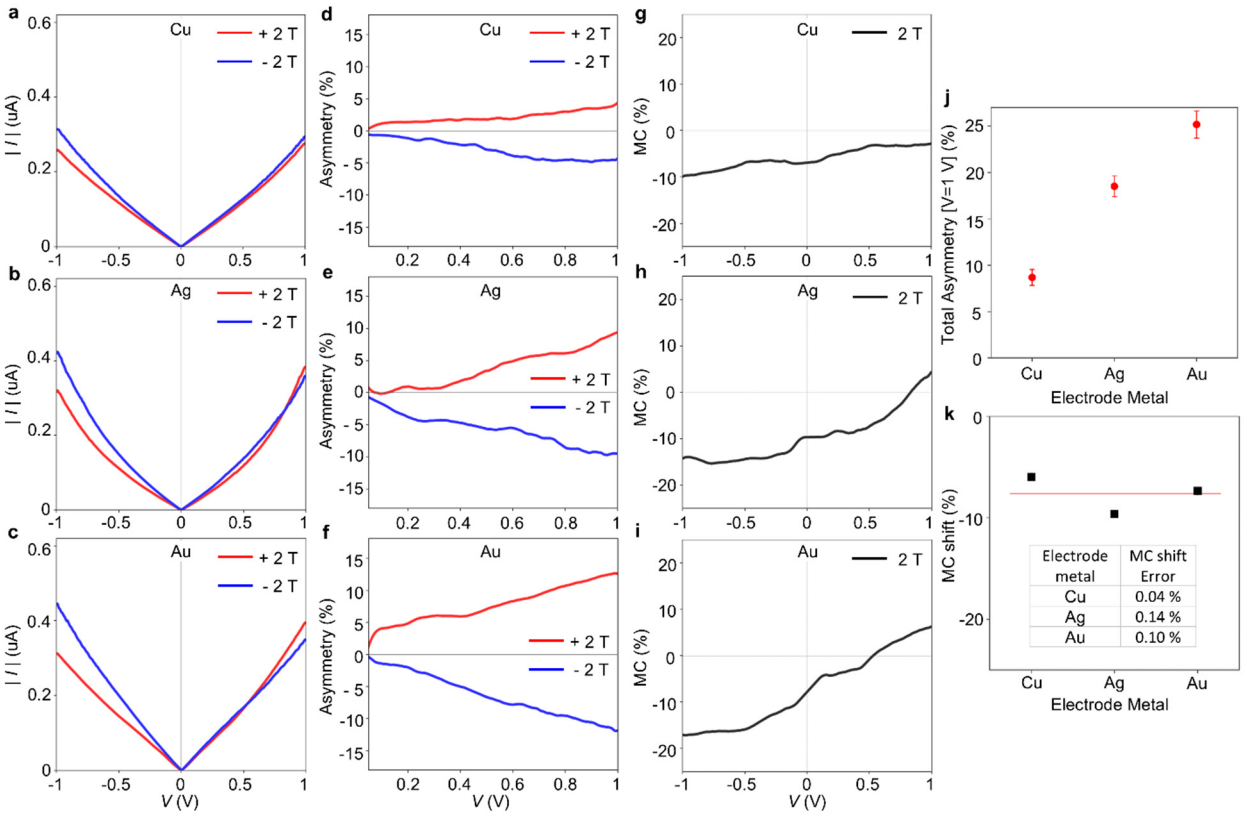

Fig. S18 | The response of asymmetry and MC to different metal electrodes for *P*-helicene based junctions. a-c, Average current (in absolute values) as a function of applied voltage for Ni(X)/P-helicene/X junctions, where X is Cu (a), Ag (b) and Au (c). The standard error of the current is smaller than the curve width. **d-f,** Average asymmetry as a function of applied voltage magnitude for the same junctions as in (a) to (c), respectively. **g-i,** Average MC as a function of applied voltage for the same junctions as in (a) to (c), respectively. **j,** Total asymmetry at 1 *V* (sum of positive and negative asymmetry magnitudes) for junctions based on different metals. **k,** MC shift (MC at zero voltage; black squares) for junctions based on different metals. The red curve represents the average value. The number of examined molecular junctions in each case varies between 248 and 448. The error bars for asymmetry and MC indicate the experimental uncertainty. See Fig. 1,g,h,k and Fig. S19, for $|I|$-V and asymmetry histograms for the Au, Cu, and Ag based junctions.

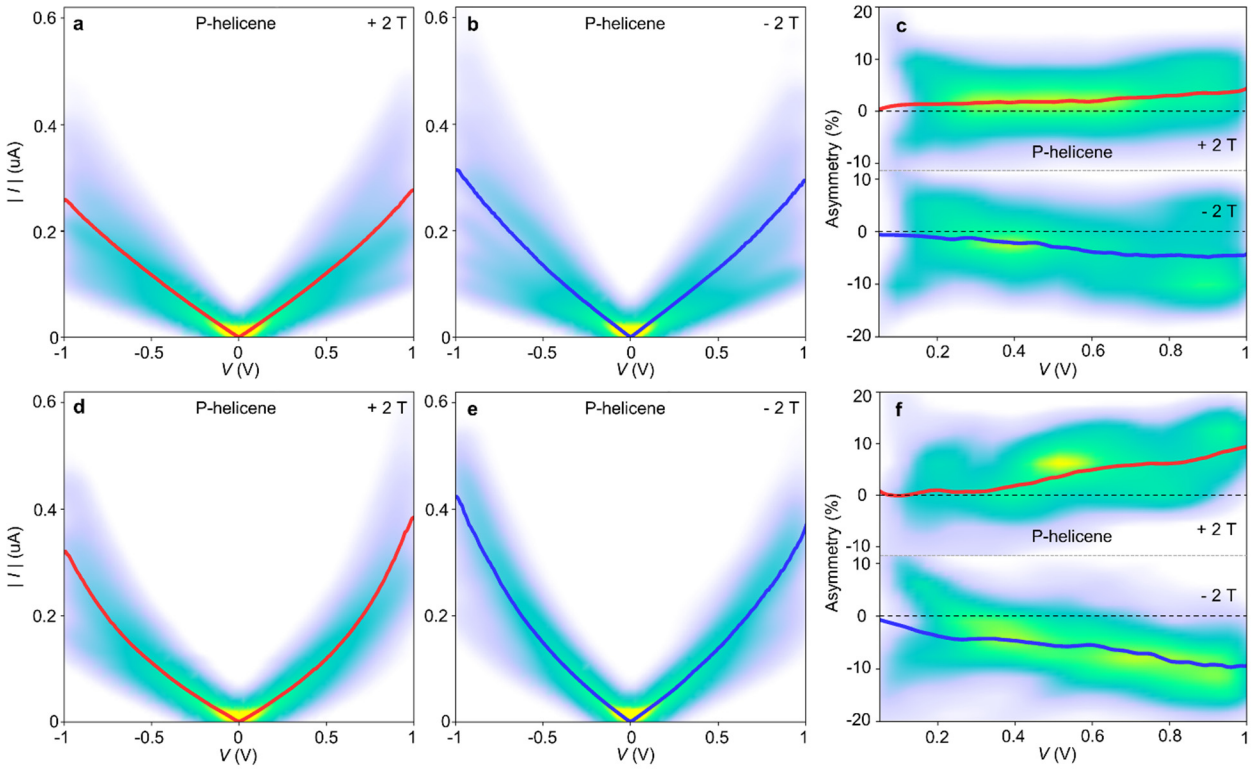

Fig. S19 | **Current versus voltage and asymmetry histograms for junctions based on P-helicene with different electrode metals. a,b,** Histogram and an average of current in absolute values as a function of voltage for Ni(Cu)/P-helicene/Cu junctions at parallel and antiparallel magnetic field orientations. The standard error of the current is smaller than the curve width. **c,** Histogram and an average Asymmetry as a function of applied voltage magnitude at parallel and antiparallel magnetic field orientations for Ni(Cu)/P-helicene/Cu junctions. **d,e,** The same as (a,b) but for Ni(Ag)/P-helicene/Ag junctions. The standard error of the current is smaller than the curve width. **f,** The same as (c) but for Ni(Ag)/P-helicene/Ag junctions. Measurements were done at an applied magnetic field of +2 **T** or -2 **T**. The number of examined molecular junctions in each case varies between 248 to 448.

References

1. Dallaire, C., Kolber, I. & Gingras, M. Nickel-Catalyzed Coupling of Aryl O-carbamates with Grignard Reagents: 2,7-dimethylnaphtalene. Org. Synth. 78, 42 (2002).

2. Minami, A., Uchida, R., Eguchi, T. & Kakinuma, K. Enzymatic Approach to Unnatural Glycosides with Diverse Aglycon Scaffolds Using Glycosyltransferase VinC. J. Am. Chem. Soc. 127, 6148–6149 (2005).

3. Mori, K., Murase, T. & Fujita, M. One-Step Synthesis of [16]Helicene. Angew. Chem. Int. Ed. 54, 6847–6851 (2015).

4. Fox, J. M., Lin, D., Itagaki, Y. & Fujita T. Synthesis of Conjugated Helical Acetylene-Bridged Polymers and Cyclophanes. J. Org. Chem. 63, 2031–2038 (1998).

5. Lai, C. & Backes, B. J. Efficient preparation of S-aryl thioacetates from aryl halides and potassium thioacetate. Tetrahedron Lett. 48, 3033–3037 (2007).

6. Stetsovych, O., Mutombo, P., Švec, M., Šámal, M., Nejedlý, J., Císařová, I., Vázquez, H., Moro-Lagares, M., Berger, J., Vacek, J., Stará, I. G., Starý, I. & Jelínek, P. Large Converse Piezoelectric Effect Measured on a Single Molecule on a Metallic Surface. J. Am. Chem. Soc. 140, 940–946 (2018).

7. Yanson, A. I., Bollinger, G. R., Van den Brom, H. E., Agrait N., Van Ruitenbeek, J. M. Formation and manipulation of a metallic wire of single gold atoms. *Nature*, **395**, 783-785 (1998).

8. Krans, J. M., Muller, C. J., Yanson, I. K., Govaert, T. C., Hesper, R. & Van Ruitenbeek, J. M. One-atom point contacts. *Phys. Rev. B.* **48**, 14721 (1993).

9. Rodrigues, V., Bettini, J., Rocha, A. R., Rego, L. G. C., & Ugarte, D. Quantum Conductance in Silver Nanowires: Correlation between Atomic Structure and Transport Properties. *Phys. Rev. B* **65**, 1–4 (2002).

10. van Ruitenbeek, J. M., Korytár, R. & Evers F. Chirality-controlled spin scattering through quantum interference. *J. Chem. Phys.* **159**, 024710 (2023).

11. Xie, Z., Markus, T. Z., Cohen, S. R., Vager, Z., Gutierrez, R. & Naaman R. Spin specific electron conduction through DNA oligomers. *Nano Lett.* **11**, 4652–4655 (2011).

12. Lu, H., Wang, J., Xiao, C., Pan, X., Chen, X., Brunecky, R., Berry, J. J., Zhu, K., Beard, M. C. & Vardeny, Z. V. Spin-dependent charge transport through 2D chiral hybrid lead-iodide perovskites. *Sci. Adv.* **5**, eaay0571 (2019).

13. Kulkarni, C., Mondal, A. K., Das, T. K., Grinbom, G., Tassinari, F., Mabesoone, M. F. J., Meijer, E. W. & Naaman, R. Highly efficient and tunable filtering of Electrons' spin by supramolecular chirality of nanofiber-based materials. *Adv. Mater.* **32**, 1904965 (2020).

14. Inui, A., Aoki, R., Nishiue, Y., Kousaka, Y., Shishido, H., Hirobe, D., Suda, M., Ohe, J., Kishine, J., Yamamoto, H. M. & Togawa, Y. *Phys. Rev. Lett.* **124**, 166602 (2020).

15. Yang, C., Li, Y., Zhou, S., Guo, Y., Jia, C., Liu, Z., Houk, K. N., Dubi, Y. & Guo X. Real-time monitoring of reaction stereochemistry through single-molecule observations of chirality-induced spin selectivity. *Nat. Chem.* **15**, 972 (2023).

16. Adhikari, Y., Liu, T., Wang, H., Hua, Z., Liu, H., Lochner, E., Schlottmann, P., Yan, B., Zhao, J. & Xiong, P. Interplay of structural chirality, electron spin and topological orbital in chiral molecular spin valves. *Nat. Commun.***14**, 5163 (2023).

17. Safari, M. R., Matthes, F., Schneider, C. M., Ernst, K. H. & Bürgler, D. E., Spin-Selective Electron Transport Through Single Chiral Molecules. *Small*, 2308233 (2023).

18. Xiao, J., Zhao, Y. & Yan, B. Nonreciprocal nature and induced tunneling barrier modulation in chiral molecular devices. arXiv:2201.03623 (2022).

19. Rikken, G. L. J. A. & Avarvari N. Comparing Electrical Magnetochiral Anisotropy and Chirality-Induced Spin Selectivity. *J. Phys. Chem. Lett.* **14**, 9727-9731 (2023).

20. Yan B. Structural Chirality and Electronic Chirality in Quantum Materials. arXiv:2312.03902 (2023).

21. Cuevas, J. C. & Scheer E. Molecular electronics: an introduction to theory and experiment. 1st Ed. World Scientific (2010).

22. Rikken, G. L. J. A., Fölling, J. & Wyder, P. Electrical magnetochiral anisotropy. *Phys. Rev. Lett.* **87**, 236602 (2001).

23. Landman, U., Luedtke, W. D., Burnham, N. A. & Colton, R. J. Atomistic mechanisms and dynamics of adhesion, nanoindentation, and fracture. *Science* **248**, 454 (1990).

24. Bhushan, B., Israelachvili, J. N. & Landman, U. Nanotribology: friction, wear and lubrication at the atomic scale. *Nature* **374**, 607 (1995).

25. Kurt, H. Ü., Chiang, W. C., Ritz, C., Eid, K., Pratt Jr, W. P. & Bass, J. Spin-memory loss and current-perpendicular-to-plane-magnetoresistance in sputtered multilayers with Au. *J. Appl. Phys.* **93**, 7918 (2003).

26. Niimi, Y., Suzuki, H., Kawanishi, Y., Omori, Y., Valet, T., Fert, A. & Otani, Y. Extrinsic spin Hall effects measured with lateral spin valve structures. *Phys. Rev. B* **89**, 054401 (2014).

27. Park, W., Baxter, D.V., Steenwyk, S., Moraru, I., Pratt Jr, W.P. & Bass, J. Measurement of resistance and spin-memory loss (spin relaxation) at interfaces using sputtered current perpendicular-to-plane exchange-biased spin valves. *Phys. Rev. B*, **62**, 1178 (2000).

28. Karube, S., Idzuchi, H., Kondou, K., Fukuma, Y. & Otani, Y. Spin relaxation characteristics in Ag nanowire covered with various oxides. *Appl. Phys. Lett.* **107**, 122406 (2015).

29. Jedema, F.J., Filip, A.T. & Van Wees, B.J. Electrical spin injection and accumulation at room temperature in an all-metal mesoscopic spin valve. *Nature,* **410**, 345 (2001).

30. Jedema, F.J., Nijboer, M.S., Filip, A.T. & Van Wees, B.J. Spin injection and spin accumulation in all-metal mesoscopic spin valves. *Phys. Rev. B*, **67**, 085319 (2003).

31. Garzon, S., Žutić, I. & Webb, R.A. Temperature-Dependent Asymmetry of the Nonlocal Spin-Injection Resistance: Evidence for Spin Nonconserving Interface Scattering. *Phys. Rev. Lett.* **94**, 176601 (2005).